VILNIUS UNIVERSITY
FACULTY OF PHYSICS
INSTITUTE OF PHOTONICS AND NANOTECHNOLOGY

Gustas Petrusevičius

CARRIER DYNAMICS IN NEUTRON-IRRADIATED GaN EPITAXIAL LAYERS

Master's thesis

(Laser Physics and Optical Technologies)

Student:	Gustas Petrusevičius
Supervisor:	Dr. Kazimieras Nomeika
Reviewer:	Prof. Dr. Vincas Tamošiūnas
Institute Representative:	Prof. Dr. Ramūnas Aleksiejūnas

Vilnius 2026

Contents

1 Abbreviations

AT	ammonothermal
BBO	β-barium borate
GaN	gallium nitride
DSP	double side polished
DAP	donor-acceptor pair
LED	light emitting diode
LD	laser diode
LITG	laser-induced transient grating
HEMT	high-electron-mobility transistor
MOVPE	metalorganic vapor phase epitaxy
$\mathbf{V}_x$	vacancy of atom X
VIS	visible (spectral range)
$\mathbf{I}_x$	interstitial
QE	quantum efficiency
UID	unintentionally doped
UV	ultraviolet (spectral range)
NIR	near-infrared (spectral range)
TIPL	time-integrated photoluminescence
RSM	reciprocal space map
XRD	x-ray diffraction
X_i	interstitial of atom X

2 Introduction

Gallium nitride (GaN) is one of the most studied group III-V semiconductors due to wide, direct bandgap, high thermal stability and breakdown field as well as rather efficient radiative recombination [1]. By compounding GaN with other III-V nitride alloys, bandgap is widely tunable, allowing to achieve a broad operational spectral range. This enables applications in optoelectronics VIS-UV range as well as in high-power electronic components. GaN-based LEDs, LDs, HEMTs are widely considered for applications not only under normal laboratory conditions, but also in harsher environments, such as space, nuclear facilities and particle physics research institutions.

For such applications the resilience of GaN must be studied. Materials tolerance becomes a critical property. Even though GaN is considered to be a rather tough and resistant material to ionizing and displacement damage, energetic particles can still modify its structural, thus electrical and optical properties [2]. High energy neutrons are especially relevant, as they primarily introduce structural displacement damage in the material. The mechanism being non-ionizing energy loss of the particles as they travel through the lattice of the material under irradiation. The displaced atoms (vacancy-interstitial pairs) act as point defects, providing non-radiative SRH recombination pathways. As a result, carrier lifetime, photoluminescence efficiency, charge transport become affected. [3]

An especially suitable platform for studying GaN irradiation effects is ammonothermally grown bulk GaN, sliced into wafers. Compared to conventional, GaN grown via metalorganic vapor phase epitaxy (MOVPE), AT GaN exhibits substantially lower dislocation densities [3]. Such a feature is highly important, as dense native defects obstruct the studies of irradiation effects by interfering with effects introduced specifically via irradiation. The contribution of neutron-induced point defect effects to carrier dynamics can be studied more clearly via the use of high-crystalline-quality AT GaN wafers instead of conventional sapphire substrates for the subsequent MOVPE epitaxial growth of GaN. However, AT GaN is not defect-free. During the growth process, various impurities such as oxygen, hydrogen, carbon, and iron can be introduced. [4, 5]. Consequently affecting the MOVPE epitaxial structures on top. So, irradiation-induced defects may still interact with already existing material native defects.

The carrier dynamics inside irradiated GaN are governed by the trapping, scattering and recombination effects. Photo-excited carriers undergo diffusion. The diffusion coefficient is sensitive to carrier mobility, doping, scattering and trapping effects. While the carrier lifetime is influenced by the recombination pathways present in the material. Therefore it provides direct information about defect-assisted recombination processes. The increase of defect states in irradiated GaN can increase the probability of non-radiative recombination, shortening carrier lifetime and reducing the distance before which carriers meet recombination sites.

Optical characterization techniques allow for contactless, non-destructive investigation of the latter carrier dynamics effects. Laser-induced transient grating (LITG) spectroscopy allows for extraction of ambipolar diffusion coefficient and carrier lifetimes via examining the decay of photo-generated carrier grating. This makes it possible to separate carrier transport from recombination effects, allowing to evaluate how irradiation modifies each contribution. While time-integrated, steady-state photoluminescence spectroscopy provides information about radiative recombination channels such as band-to-band and radiative SRH recombination. In GaN, photoluminescence (PL) is particularly sensitive to defect-related states in the bandgap, making PL spectroscopy a useful tool for evaluating the competition between different recombination channels as well as the quantum efficiency. Enabling a quantitative comparison of radiative efficiency among the samples [6].

The aim of this work is to investigate the influence of neutron irradiation on charge carrier dynamics and recombination processes in epitaxial GaN layers grown via MOVPE on top of AT GaN wafers. For this purpose, a set of GaN samples irradiated with neutron-equivalent doses ranging from $1 \cdot 10^{12}$ to $1 \cdot 10^{17}$ $\frac{neq}{cm^2}$ was studied. Laser-induced transient grating spectroscopy was used to determine the ambipolar diffusion coefficient and carrier lifetime as functions of excitation fluence and irradiation dose. Photoluminescence spectroscopy was used to evaluate changes in emission spectra and photoluminescence quantum efficiency. By combining these methods, this work seeks to determine how neutron-induced defects affect carrier transport, recombination efficiency, and the optical degradation of AT-MOVPE-GaN.

This study is relevant for both fundamental and applied semiconductor physics. From a fundamental perspective, it provides insight into how irradiation-induced point defects and defect complexes influence carrier transport and recombination in high-crystalline-quality GaN. From an applied perspective, it contributes to the assessment of GaN suitability for devices intended to operate in harsh, radiation-rich environments. Understanding which carrier-dynamic parameters are most strongly affected by neutron irradiation is necessary for improving GaN-based materials and designing devices with enhanced radiation hardness.

3 Literature Overview

3.1 Group III-V Nitrides

Aluminum nitride (AlN), indium nitride (InN) and gallium nitride (GaN) comprise a well-known wide-bandgap semiconductor group that is widely used in various optoelectronic devices as well as high-power electronic devices [7]. An industry-standard method of group III-V nitride epitaxial growth is metalorganic vapor phase epitaxy (MOVPE) [8]. It allows to alloy the latter materials into ternary and quaternary compounds such as InGaN, AlGaN or AlInGaN, and facilitates continuous bandgap tuning from 0.7 eV (InN) up to 6.2 eV (AlN) [9].

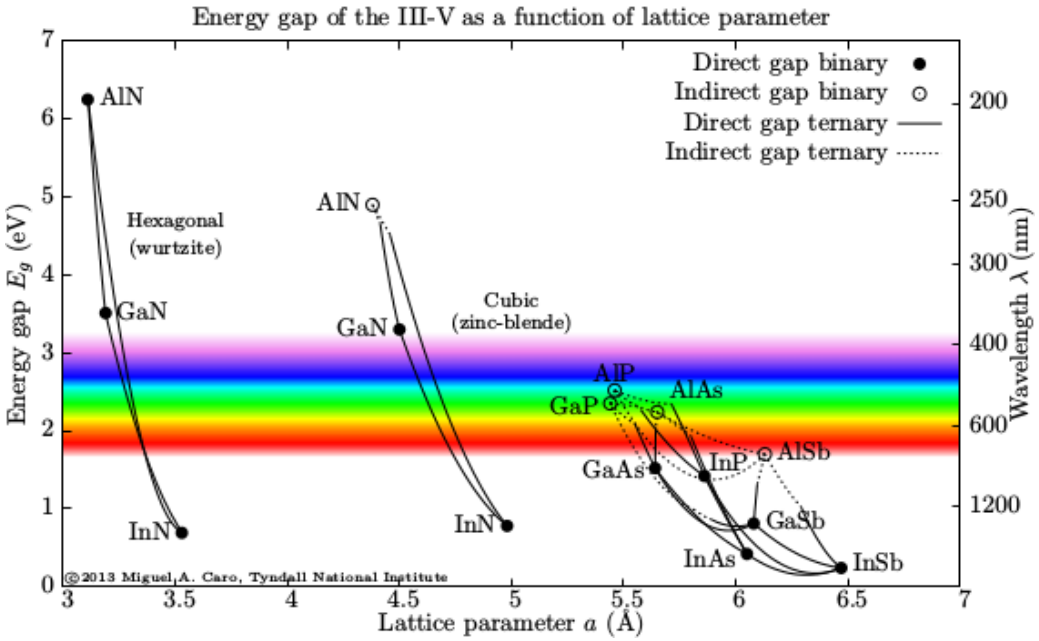

Figure 1: Bandgap energies and lattice parameters of group III-V nitrides and related compounds [10].

Such tunability allowed for the development of various devices operating in the UV and visible spectral range, e.g. blue and green LEDs and LDs. Of III-nitride semiconductor family, GaN has a direct bandgap of 3.4 eV, as well as radiative transfers of high efficiency even at elevated temperatures and high breakdown voltages [11]. Such characteristics made it suitable for various successful and wide-spread applications. One of which was the development of white-light GaN LED-based sources when coupled with phosphor coatings [12].

However, for applications in harsher conditions, such as outer space, the resilience of GaN sparks further interest. Even though GaN is often regarded as one of the more radiation-tolerant semiconductors, energetic particles can still introduce various structural defects into the lattice of GaN [13].

3.2 Ammonothermal GaN Growth

To study the influence of neutron irradiation to the lattice of GaN, ammonothermal GaN is widely used. Using ammonothermal GaN growth method, significantly lower dislocation densities are achieved (typically $10^4\,\mathrm{cm}^{-2}$). On the contrary, in HVPE GaN, dislocation densities reach $\geq 10^6\,\mathrm{cm}^{-2}$ and $\geq 10^9\,\mathrm{cm}^{-2}$ in MOVPE-grown epitaxial GaN layers [3].

Ammonothermal GaN growth is a high-pressure, solution-based bulk crystal growth technique. The growth procedure involves dissolution, transport and recrystallization of GaN in supercritical ammonia, inside a high-pressure autoclave [4, 14]. The growth principle is depicted in Figure 2.

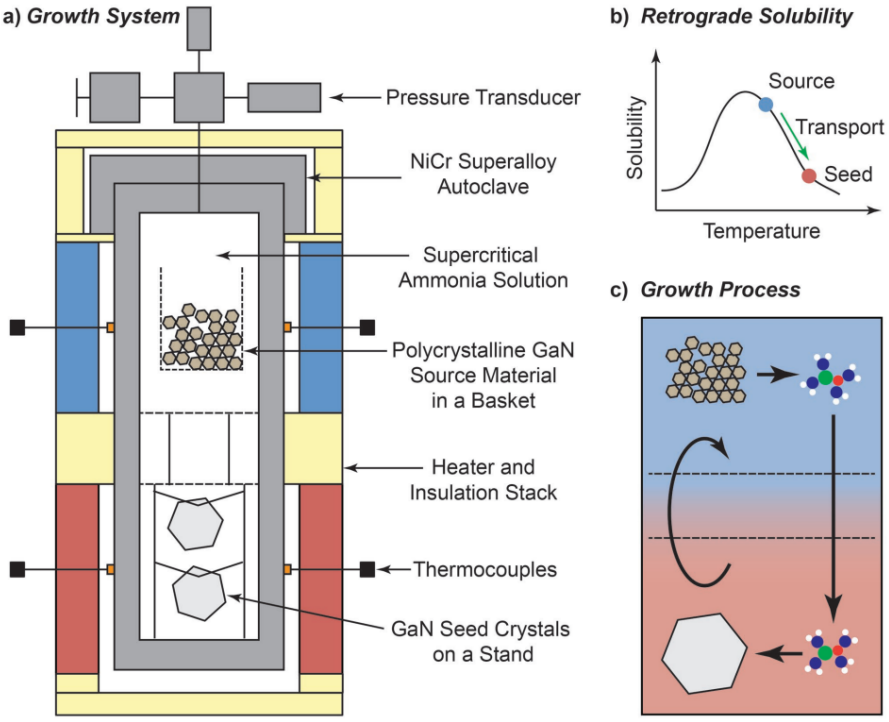

Figure 2: Schematic working principle of ammonothermal GaN growth [14].

Gallium nitride is dissolved in the supercritical ammonia. The growth vessel is divided into a *dissolution zone*, that contains the dissolved GaN (the feedstock), and the *recrystallization zone*. The latter contains the GaN seed crystals. The two regions are maintained at different temperatures due to separate heaters. Baffles are used to divide the regions and control the convective flow of GaN feedstock towards the seed. In the growth region, supersaturation is achieved and GaN precipitates epitaxially onto the seed crystals. Typical operating conditions are 400-600 $°C$ at 0.1-0.3 GPa of pressure [4]. Such conditions are able to keep the ammonia in its supercritical state and maintain a slow, near-equilibrium crystal growth. So, the ammonothermal growth method is driven by high-pressure dissociation in a solvent, thermal mass transport and recrystallization onto

seeding crystals. All to produce thick (bulk) GaN as homogeneous single crystals [4].

It is important to minimize the density of "native" dislocations in the virgin material before irradiation process. It allows to study how the radiation affects the carrier dynamics and recombination processes more clearly, without the abundance of intrinsic defects in the material, formed during epitaxial growth. Therefore ammonothermal GaN wafers were chosen as the substrate instead of the usual sapphire for MOVPE GaN growth, producing the samples investigated in this work.

3.3 Neutron-irradiated GaN

The resilience of GaN is studied by the means of neutron irradiation of varying density. Fast neutrons damage the lattice by mainly creating various displacement defects. In literature, anisotropic lattice damage is observed mainly along the c-axis of the crystal, while in-plane lattice parameter shows no significant change [5].

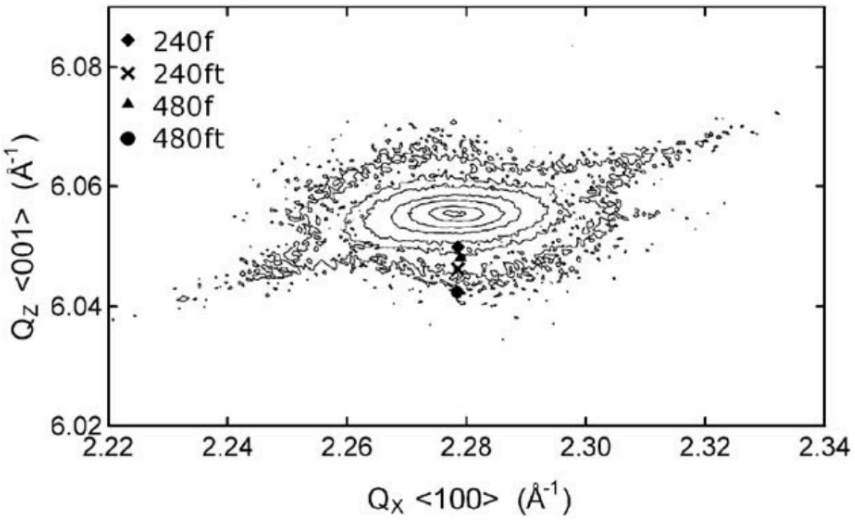

Figure 3: XRD RSM plot of GaN layers that were irradiated with neutrons for 240 and 480 hours. Letter "f" denotes "fast" neutrons, while the letter "t" denotes "thermal" neutrons. It shows that neutron irradiation shifts the GaN diffraction peak mainly along Q_z direction (corresponding to c-axis). Hence it indicates that the irradiation-induced defects produce an increase in the c-lattice parameter, while the in-plane lattice parameter remains unaffected. [5].

J. G. Marques et. al. performed XRD measurements and quantitatively demonstrated the increase of c-lattice parameter, while the a-lattice parameter remains unchanged in neutron-irradiated GaN samples (see Table 1).

Table 1: Measured lattice parameters from the XRD experiments for as-grown (virgin) and neutron-irradiated GaN samples [5].

Measured Lattice Parameters		
Sample	a **(Å)**	c **(Å)**
Virgin	3.1850	5.1881
240f	3.1843	5.1929
480f	3.1837	5.1945
240ft	3.1842	5.1960
480ft	3.1848	5.1996

Neutron irradiation affects not only the crystalline structure of GaN, but also the optical response by creating various radiation-induced defect states into the bandgap. The latter emerge from point defects and defect complexes, scattered along c-axis of GaN. Such defects act as trapping, scattering and recombination centers and in turn modify the balance between radiative and non-radiative carrier recombination processes. As a result, a common trend of carrier lifetime reduction and the decrease of photoluminescence efficiency - an overall degradation of optical performance - is observed in literature [3].

Therefore, the study of neutron-irradiated GaN provides important insight into the limits of its material resilience and its suitability for use in harsh environments.

3.4 Defects in Ammonothermal GaN

Although the ammonothermal growth procedure ensures superior crystalline quality of GaN compared to other epitaxial growth techniques, the produced material is far from defect-free. Various defects can still be introduced into the lattice throughout the growth process due to non-ideal thermodynamic conditions, present residual impurities or later by irradiation process [3, 14]. All these defects reduce structural, and thus electrical and optical properties of GaN. They act as scattering, doping, trapping and non-radiative recombination sites. When studying the effects of irradiation to GaN material, defects play the major role in explaining and characterizing the charge carrier behavior in the material. This section delves deeper into different types of defects, that appear in GaN during ammonothermal growth, as well as during irradiation process and their influence to charge carriers.

3.4.1 Impurity Incorporation

Incorporation of impurities during ammonothermal growth process arises from the closed growth chamber. Residual contamination of the chamber surfaces may be present, as well as impurities in precursor materials such as mineralizers and hydrogen. The

main impurities observed in ammonothermal GaN include hydrogen and oxygen. Oxygen increases the free-electron concentrations, as it acts as a shallow donor. It is responsible for reducing the transparency of the crystal due to induced sub-bandgap absorption through phonon-assisted processes. Oxygen can also form complexes with V_{Ga}. While hydrogen incorporates as a mobile interstitial defect, in turn participating in passivation of electrically active centers and vacancy-complex formation. Typical concentrations of hydrogen and oxygen, found in ammonothermal GaN are $\sim 10^{17} - 10^{19}$ cm^{-3}. [14]

Na, Fe, Mn are also relevant as they appear due to residual contaminants (Fe, Mn) and the use as mineralizers (Na). They introduce deep states within the bandgap of GaN and act as efficient SRH recombination sites [14]. Residual C is also found in ammonothermally-grown GaN, acting as a compensating acceptor and contributing towards the well-known yellow-luminescence (YL) line [15].

3.4.2 Growth-sector Inhomogeneity

A distinct characteristic of ammonothermally grown GaN that separates it from its epitaxial counterparts is the presence of growth sectors. Due to the anisotropy of GaN growth, the crystal incorporates impurities at different rates across different regions. For example in +c and -c directions and lateral wing regions. So, the concentration of defects is not uniform across the grown structure. Therefore the different growth sectors are visible optically, as different regions exhibit uneven impurity and thus free-carrier concentrations. In ammonothermal GaN this is especially apparent with oxygen incorporation as order of magnitude incorporation inhomogeneities across c and a crystallographic directions are reported in literature. Thus growth sector inhomogeneity is the dominating structural defect mechanism in ammonothermal GaN growth process. [14]

3.4.3 Gallium Vacancies

The most prominent point defect in GaN are gallium vacancies V_{Ga}. Typical V_{Ga} densities found in AT GaN reach 10^{18} cm^{-3}, several orders of magnitude higher than in HVPE-grown GaN [14]. Positron annihilation measurements performed by *Heikkinen et. al.* show clear carrier trapping at V_{Ga}-related defects in as-grown GaN [16]. However, the same study reports that as-grown UID AT GaN is of n-type regardless of high V_{Ga} acceptor densities [16]. Electron densities of UID AT GaN reaching $10^{18} - 10^{19}$ cm^{-3}, are attributed to high concentration of incorporated oxygen [16].

3.4.4 Impurity-related Defects and Complexes

Hydrogenated gallium vacancies ($V_{Ga} - H_x$) are particularly abundant in AT GaN. They naturally form in hydrogen-rich ammonothermal growth environment. Calculations by *Suihkonen et. al.* showed that $V_{Ga} - H_{1,\,2}$ are acceptor-type defects with energy levels

0.8 eV above the valence band, whereas $V_{Ga} - H_3$ is neutral and $V_{Ga} - H_4$ is unstable in typical n-type conditions [14]. Due to the abundance of hydrogen during growth, it is believed that most V_{Ga} in as-grown AT GaN are likely hydrogenated rather than isolated [16].

3.5 Defects in Irradiated GaN

Irradiation with energetic particles introduces additional defects into the lattice of GaN. This section delves deeper into the defect types and their effects.

3.5.1 Point Defects

GaN irradiation with energetic particles (neutrons) primarily creates point defects in the lattice [3]. The mechanism behind the creation of point defects being non-ionizing energy loss (NIEL). Meaning that as energetic particles pass through the lattice of GaN, they displace the atoms without creating ion pairs [3]. So, one of radiation damage manifestations in GaN is the creation of vacancy-interstitial pairs, which in turn modify the electronic structure of the material by introducing energy states in the bandgap. Electron spin resonance measurements performed by *Gaubas et. al.* revealed the appearance of radiation-induced defect signals at higher neq doses [3]. Thus indicating the formation of point-defect-related centers after irradiation. Reduction in carrier lifetime and changes to luminescence properties were observed [3].

3.5.2 Complex Formation

Upon irradiation, the generated point defects do not necessarily remain isolated. They can interact with the already present native defects in the material from ammonothermal growth process (as discussed previously). In particular, electron spin resonance measurement technique shows the formation of gallium-vacancy-oxygen complex $V_{Ga}O_N$ [3]. Furthermore, FTIR measurements show vibrational mode signatures of gallium-vacancy-multihydrogen complexes, meaning that they remain present in the material even after irradiation [3]. These observations show that irradiation in ammonothermal GaN leads to an evolution of complex defect configurations involving vacancies and residual impurities such as oxygen, hydrogen and carbon.

3.6 Charge Carrier Dynamics in GaN

For LITG characterization of irradiated GaN, it is important to understand the basic charge carrier dynamics in the material. This section explains how the generated non-equilibrium charge carriers interact with each other and traverse across the material.

3.6.1 Ambipolar Diffusion

Upon photo-excitation, a gradient of excited charge carriers is generated. In turn, they diffuse. The diffusion coefficient is different for both generated holes and electrons. Thus it is defined as ambipolar diffusion. The latter occurs when holes and electrons are coupled under an internal electric field (called Dember field) that arises from the difference of their mobilities. As a result, electrons and holes move together with an effective ambipolar diffusion coefficient D_a, given by:

$$D_a = \frac{n+p}{\frac{n}{D_h} + \frac{p}{D_e}}, \tag{1}$$

where n and p are the electron and hole concentrations respectively, D_e and D_h are the their corresponding monopolar diffusion coefficients. From the above-mentioned equation one can see that in a hole-rich system, in the low-injection regime, D_a becomes strongly dependent on the electron diffusion properties. Large hole population forms a large background reservoir. The optically generated electrons are the limiting minority carriers. Since the hole population is already large, the excess generated carriers effectively follow the diffusion of minority electrons. *Vice versa* is true for an electron-rich system.

By rewriting eq. (1), one can estimate the equilibrium charge carrier densities p_0 or n_0 by fitting the ambipolar diffusion dependence on photo-excited carrier concentration n_{ex}:

$$D_a(n_{ex}) = \frac{n_0 + p_0 + 2n_{\mathrm{ex}}}{\frac{n_0+n_{ex}}{D_h} + \frac{p_0+n_{\mathrm{ex}}}{D_e}} \tag{2}$$

It is important to note, that both monopolar diffusion coefficients depend on doping densities due to ionized impurity scattering, effective mass changes (due to Fermi level shift), increased recombination rates due to defect formation.

3.6.2 Parametric Ambipolar Diffusion Analysis

A parametric analysis of eq. (2) was carried out. The GaN absorption coefficient at 340 nm (excitation wavelength used) $\alpha = 9 \cdot 10^4$ cm^{-1} was obtained from literature [17]. It is important to note that the electron and hole mobilities, and consequently diffusivities depend on incorporated impurity concentrations during growth. So, charge carrier diffusivities cannot be fixed and their dependence on doping concentration must be accounted for. Hole and electron mobilities were obtained from [18]. Recalculated to diffusivities using Einstein's relation:

$$D = \frac{\mu k_B T}{q} \tag{3}$$

The results of parametric eq. (2) analysis are presented below:

In n-GaN ambipolar diffusion coefficient reduces with injected carrier density. While

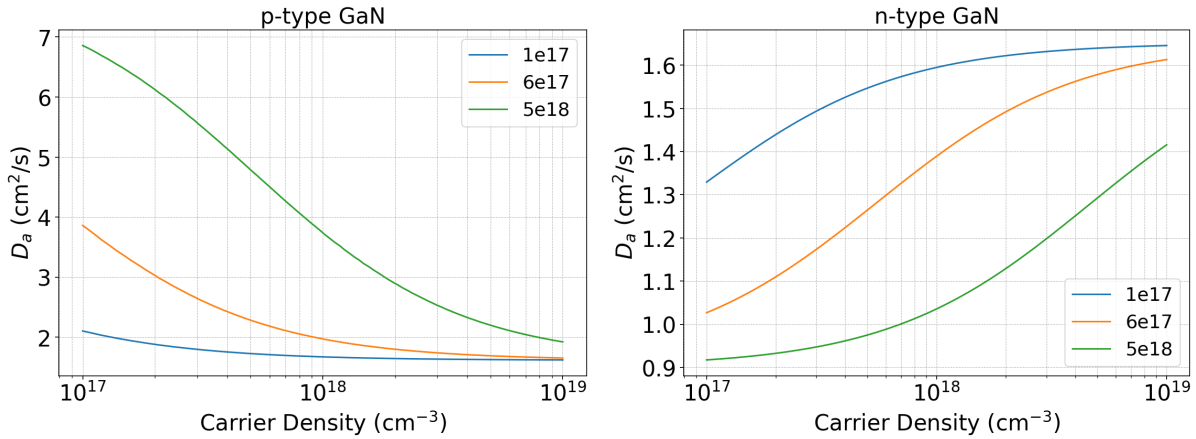

Figure 4: Theoretical ambipolar diffusion coefficient dependence on excited carrier densities for p-type and n-type GaN. Left graph represents the dependence of ambipolar diffusion coefficient on non-equilibrium carrier density in p-GaN at different hole concentrations. Right graph shows how the ambipolar diffusion coefficient behaves in n-GaN at different n-type doping concentrations.

in p-type GaN it is expected to see an increase in ambipolar diffusion coefficient at low non-equilibrium carrier densities. This can be observed from eq. (2) analysis. Equilibrium hole concentration p_0 is significantly larger than n_0. D_h is lower than D_e [19]. As n_{ex} approaches equilibrium carrier densities, carrier populations begin to symmetrize. Contribution from the faster moving electrons increases and ambipolar diffusion coefficient is increased. At high injection regime ($n_{ex} >> p_0, n_o$), ambipolar diffusion approaches $2D_h$, as $D_h << D_e$.

So, by obtaining the ambipolar diffusion on excitation fluence (excited carrier density) dependence and inspecting the shape of the curve, it is possible to estimate the doping type of the material.

3.6.3 Charge Carrier Scattering

Charge carrier lifetime and mobility in a semiconductor are of utmost importance for electrical applications [20]. Charge carrier scattering limits the mobility and lifetime therefore it affects the conductivity of the device. Charge carrier scattering is an indicator of material quality. A material of fewer electrically active defects will exhibit weaker carrier scattering. In MOVPE GaN grown on AT GaN wafers, scattering effects are less dependent on extended defects such as threading dislocations, and more governed by the extent of point defects and impurities [21]. Although it was believed that the dominant scattering mechanism in GaN were the abundant $V_{Ga} - H - O$ (hydrogenated Ga-vacancy complexes), *Jiang et. al.* showed that they do not strongly affect carrier mobility [21]. Hence, the main scattering centers in GaN are believed to be residual impurities such as oxygen and hydrogen [3].

Irradiation process increases charge carrier scattering. It introduces additional point

defects and defect complexes into the lattice (as discussed previously). Hence, the density of carrier scattering sites is increased. As a result, irradiation not only shortens the carrier lifetime but in turn degrades carrier transport as well. So, it is important to study the extent of GaN resilience for harsh applications.

3.7 Charge Carrier Recombination Pathways in GaN

This section delves deeper into the possible photoexcited charge carrier recombination pathways, present in GaN. This is particularly important when trying to understand certain photoluminescence behavior of GaN samples of neutron-equivalent irradiation densities. Upon photo-excitation an electron-hole pair is generated in GaN. There are multiple competing recombination pathways:

- Radiative recombination. Most probable radiative recombination path involves recombination of free electron and hole pair during the so-called band-to-band recombination process. Such process is rather probable in GaN layers of high crystalline quality and is essential for the operation of active optical devices such as LEDs and LDs [22]. It produces a characteristic GaN photoluminescence line, centered at around 364 nm (or 3.4 eV) [23]. Strong band-to-band photoluminescence emission is the usual indicator of good crystalline quality of the structure.

- Shockley-Read-Hall (SRH) recombination. This is the main recombination mechanism observed in highly irradiated GaN [3]. Irradiation process generates high density of defect-related energy levels within the bandgap. In this process, charge carriers are captured by these trap states and non-radiatively recombine via phonon emission. The probability of SRH recombination increases strongly with defect concentration, making it particularly important after neutron irradiation, where vacancy-related complexes, interstitials, and other deep-level centers act as efficient recombination sites. SRH suppresses the band-to-band emission in highly irradiated GaN samples and is mainly responsible for the degradation of total luminescence. [24]

- Auger-Meitner recombination. It is a three-carrier interaction process in which an excited charge carrier non-radiatively recombines by transferring its excitation to another carrier, promoting it to a higher energy level. The process can be of two types: npp and npn. In the npp process, the third carrier is a hole (it involves one electron and two holes), meaning the recombination energy boosts another hole deeper into the valence band. In the npn process, the third carrier is an electron (it involves two electrons and one hole), meaning the energy is given to an electron pushed higher into the conduction band. In n-type materials (such as UID GaN) npn process tends to dominate. Auger-Meitner recombination does not contribute to the total emitted PL. [25]

- Trap-assisted Auger-Meitner recombination. It is facilitated by the presence of a defect state. Charge carriers recombine through the latter trap state, transferring the energy to a third free carrier rather than emitting a photon. The energetic carrier then subsequently relaxes via phonon emission, converting the excitation energy into heat. Thus it is also a non-radiative recombination process, without contribution to total emitted PL. [25]

All abovementioned photoexcited carrier recombination processes are illustrated in Figure 5.

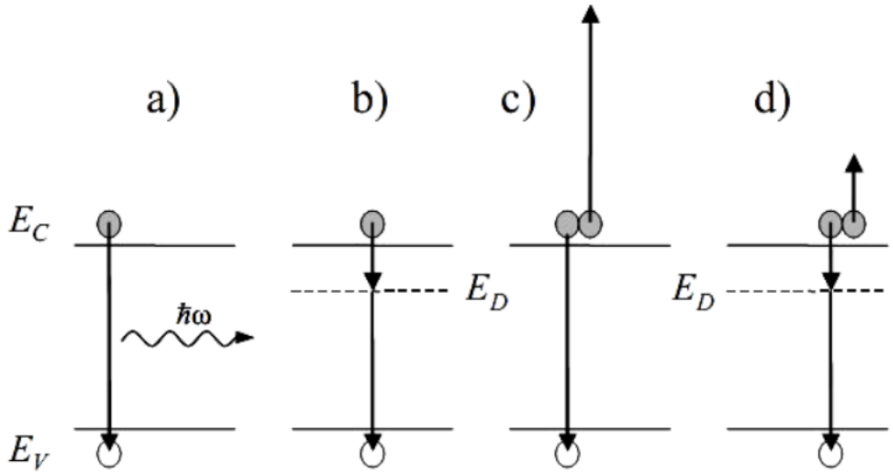

Figure 5: Energy diagram depiction of various recombination processes: a) radiative recombination, and three non-radiative recombination mechanisms: b) SRH recombination, c) Auger-Meitner recombination, d) trap-assisted Auger-Meitner recombination. [25].

3.8 Photoluminescence of GaN

By measuring and analyzing the photoluminescence spectrum of the sample, various charge carrier relaxation pathways are probed. Under optical excitation, electrons are promoted to higher-energy states and subsequently relax through a combination of radiative and non-radiative processes, as shown in Figure 6. The emitted photoluminescence spectrum reflects the competition between these channels and can be used to attribute optical behavior to specific electronic transitions. In wide-bandgap GaN, PL is particularly sensitive to defect and dopant related states within the bandgap [26]. Thus making it a suitable tool for assessing the quality of GaN where impurity incorporation strongly influences the recombination mechanisms.

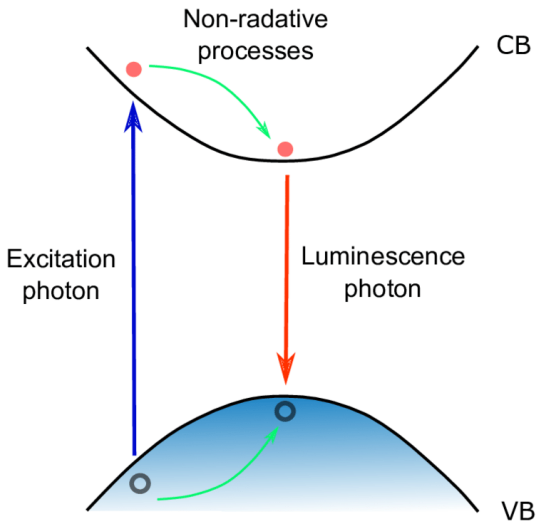

Figure 6: Mechanism of photoluminescence emission [15].

In irradiated GaN, PL can be used to assess changes in the defect density. By analyzing both the intensity and spectral distribution of the luminescence. The irradiation-induced defects create additional trap states and non-radiative recombination sites, thus typically reducing the near-band-edge emission intensity while promoting defect-related bands corresponding to red-shifted PL emission. Thus a systematic evaluation of PL spectra with increasing density of irradiation provides indirect information about the generation of defects.

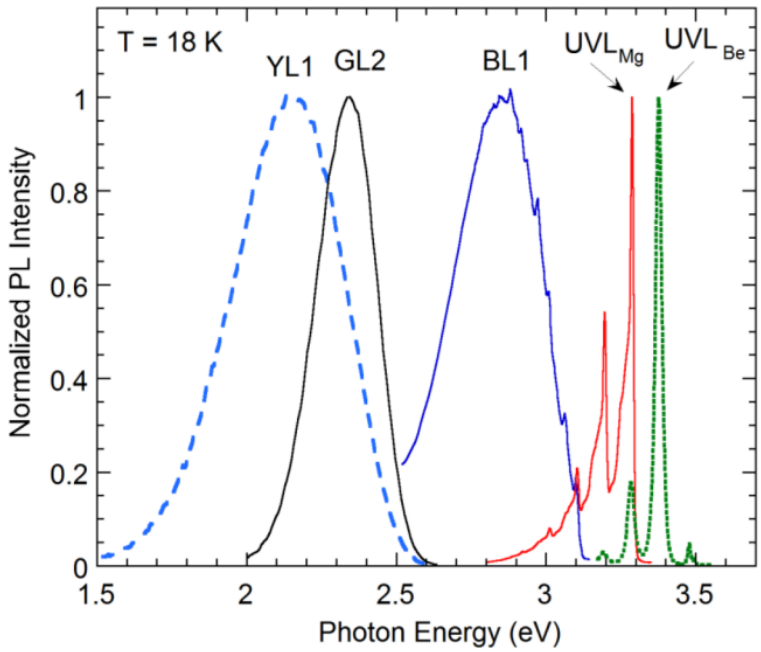

Figure 7: Typical defect-related PL bands in GaN [6].

The most common defect-related PL bands observed in GaN (depicted in Figure 7) can be summarized as follows:

- **Yellow luminescence (YL).** The YL1 band is typically observed around 2.1–2.3 eV and is one of the most common defect-related bands in unintentionally doped n-type GaN. It is commonly associated with deep acceptor-like defects, especially carbon on the nitrogen site C_N and gallium vacancies V_{Ga}. They provide deep energy states above the valence band through which carriers in shallow donor states near the conduction band, present due to Ga_i and N_V defects can recombine as donor-acceptor pair (DAP). [27]

- **Green luminescence (GL).** The GL2 band appears around 2.3–2.5 eV and is related to similar deep defect states in the GaN bandgap. However, it is often observed in compensated or semi-insulating GaN and may involve similar V_{Ga} defects or $V_{Ga} - donor$ (such as $V_{Ga} - O_N$) defect complexes. [28]

- **Blue luminescence (BL).** The BL1 band is usually centered around 2.8–3.0 eV. It is often attributed to impurity-related acceptor states, particularly Zn_{Ga}, when zinc is unintentionally incorporated into the material. However, it can also arise from unintentional carbon incorporation as a result of C_{Ga} (shallow donor) - C_N (shallow acceptor) DAP recombination. [29]

- **Acceptor-related ultraviolet luminescence (UVL).** UVL_{Mg} and UVL_{Be} are near-band-edge acceptor-related transitions observed in Mg or Be-doped GaN. The latter create shallow acceptor energy states. In unintentionally doped GaN, these lines are mainly used as reference transitions and are not expected to dominate unless such impurities are present. [30, 31]

In the context of the investigated irradiated GaN samples, the most relevant PL spectral features are the near-band-edge emission around 3.4 eV and the broad defect-related visible emission, especially the YL region. Changes in these bands reflect the competition between radiative band-edge recombination, defect-assisted radiative recombination, and non-radiative recombination through irradiation-induced defect states.

4 Research Methodology

To probe and investigate the effects of the lattice damaging neutron irradiation, optical characterization techniques prove to be especially useful. PL can reveal changes in radiative recombination and emission efficiency, while light-induced transient grating (LITG) spectroscopy measurements provide insight into the carrier transport and recombination parameters such as ambipolar diffusion and carrier lifetimes. By investigating how these

quantities change with varying neutron irradiation density, it becomes possible to assess the extent to which irradiation-induced defects influence the carrier dynamics in the epitaxial layers of GaN.

This section presents the methods of neutron-irradiated GaN measurements. The investigated sample set, experimental setups and their theoretical backgrounds are presented.

4.1 Investigated Samples

In this work, a series of irradiated epitaxial MOVPE GaN layers grown on top of ammonothermal GaN substrate is investigated. A single ammonothermal growth process was carried out, producing a mono-crystalline bulk GaN, which was cut into c-plane AT GaN wafers of high crystalline quality (exhibiting previously discussed features in the literature overview section). Subsequently, a single GaN MOVPE growth was performed, producing a wafer of epitaxial GaN atop AT GaN substrate. For simplicity the entire sample with MOVPE GaN on top will still be referred to as "AT-MOVPE-GaN". The latter was cut into 6 pieces. They were irradiated by varying amounts of $\frac{neq}{cm^2}$ dose. The set of investigated samples are presented in Table 2 and the considered dose severities in Table 3. The schematic depiction of the samples is shown in Figure 8.

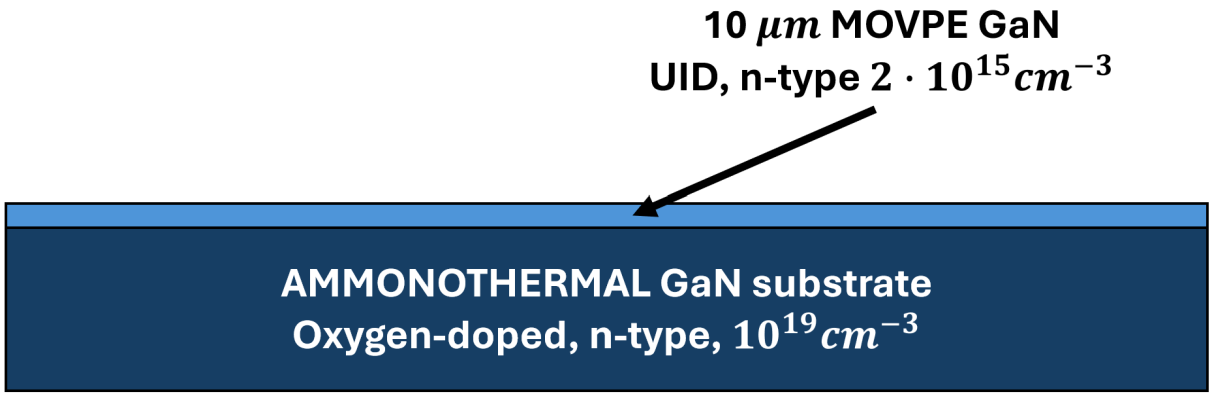

Figure 8: Schematic representation of the investigated AT-MOVPE-GaN sample structure.

4.2 Laser-induced Transient Grating Spectroscopy

LITG is a contactless optical technique for probing both transport and recombination dynamics of photoexcited carriers in semiconductors. Regarding p-GaN, it is especially valuable as conventional electronic methods are challenging due to poor ohmic contact formation and various parallel conductivity pathways.

Table 2: The investigated sample set with corresponding irradiation doses.

Sample Set	
Sample Name	**Irradiation Dose ($\frac{neq}{cm^2}$)**
Sample A	1×10^{12}
Sample B	1×10^{13}
Sample C	1×10^{14}
Sample D	1×10^{15}
Sample E	1×10^{16}
Sample F	1×10^{17}

Table 3: Naming convention used to refer to the extent of radiation samples have received.

Sample	**Dose Severity**
A–B	Mild
C–D	Moderate
E–F	Heavy

4.2.1 Principle of Operation

LITG measurement technique is based on four-wave mixing - a third-order nonlinear process. A fourth wave is produced by the three interacting waves. The resulting waves amplitude is governed by:

$$P_i^{(3)}(\omega_4) = \chi_{ijkl}^{(3)} E_j(\omega_3) E_k(\omega_2) E_l(\omega_1), \tag{4}$$

where $P_i^{(3)}(\omega_4)$ is the third-order polarization amplitude of the frequency ω_4, E_j, E_k, E_l are the electric field amplitudes of the impinging waves, and lastly, $\chi_{ijkl}^{(3)}$ is the $ijkl$ element of the third-order susceptibility tensor. The principle schematic of all four waves is shown below:

4.2.2 Grating Formation

The sample is excited with two coherent pulses of the same amplitude, of the wavelength in the absorption range. If the delay between the exciting pulses is lower than the phase relaxation time, an interference pattern - excitation grating is created in the sample. The intensity distribution in the interference region of the two interacting excitation pulses is given by:

$$I(x) = 2I_{\text{exc}} \left[1 + \cos\left(\frac{2\pi x}{\Lambda} \right) \right], \tag{5}$$

where Λ is the induced grating period, λ_{exc} is the wavelength of the excitation pulses, and I_{exc} is the intensity of one of the exciting pulses. The grating period Λ is given by:

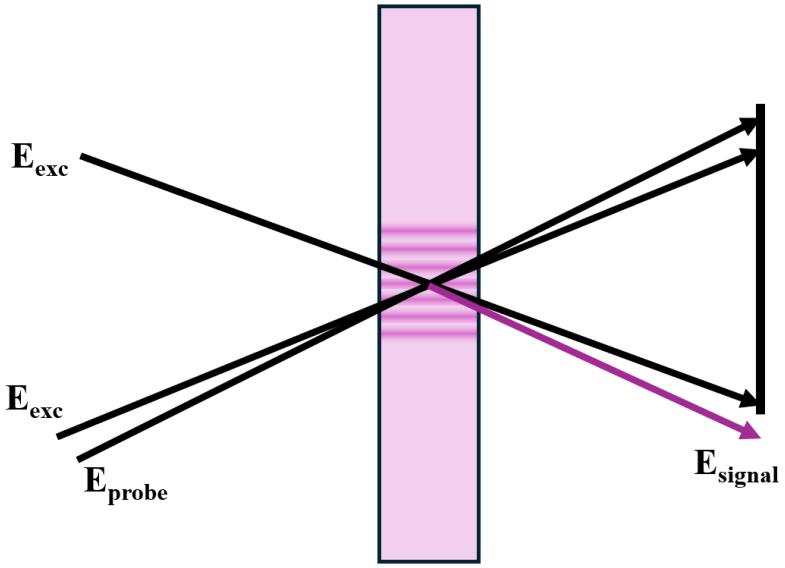

Figure 9: Principle of laser-induced transient grating on the sample. E_{exc} are the excitation waves, E_{probe} is the temporally delayed probing pulse, and the E_{signal} is the resulting detected diffracted probe.

$$\Lambda = \frac{\lambda_{exc}}{2\sin\left(\Theta/2\right)}. \tag{6}$$

Meaning that the period of the induced structural excitation depends on the distance (or the angle) between the exciting pulses (as shown in Figure 10). The smallest angle between the excitation pulses will result in the largest period of the induced excitation grating. Similarly, the largest distance (or the largest angle) between the exciting pulses will result in the smallest grating period. Such grating is purely an electronic grating - a carrier density modulation. Which in turn creates a refractive index variation.

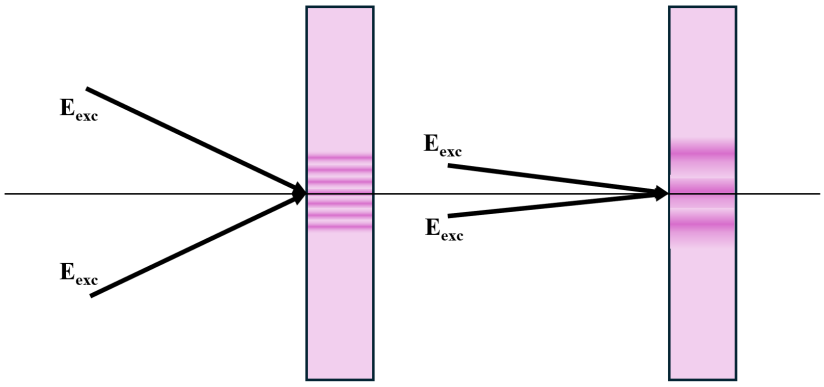

Figure 10: Induced structural excitation of the sample depending on the angle between exciting pulses.

The third, probing pulse, which is of longer wavelength (so that it is in the transmission region of the sample) will consequently diffract from the induced transient grating.

4.2.3 Measurement Setup

I-OPA - a parametric amplifier coupled to Carbide laser (by *Light Conversion*) was used to provide both exciting and probing beams. Harpia-TG was used to carry out LITG measurements for all samples. 1030 nm wavelength probe together with 340 nm excitation beam was used throughout this work. The measurement setup used in this work is presented in Figure 11.

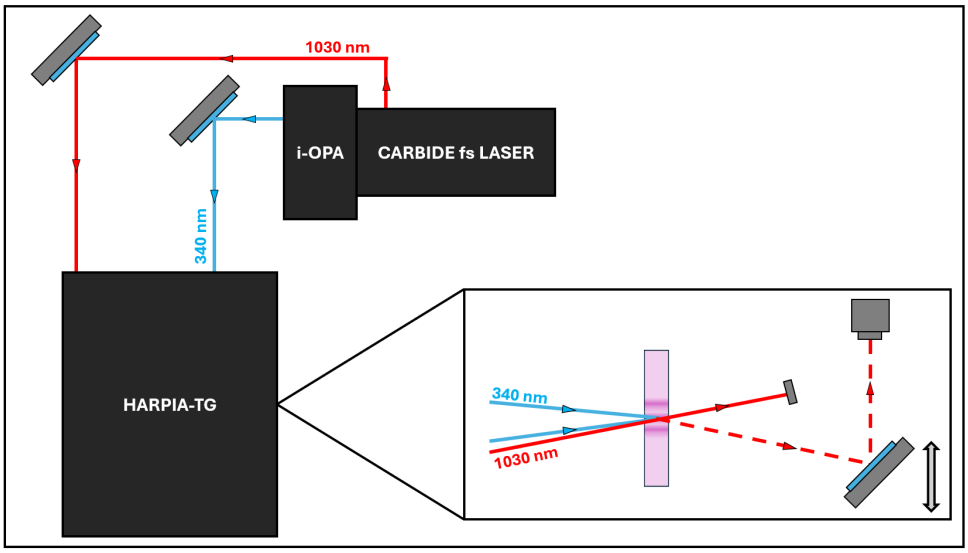

Figure 11: Schematic illustration of the used LITG measurement setup.

4.2.4 Data Interpretation

As the sample is excited with two UV excitation pulses, forming a transient grating, a third pulse - the probe is optically delayed and allowed to diffract from the grating. The detected diffracted probe intensity is plotted against time delay, constructing the kinetic trace of diffracted probe intensity. The diffraction signal decay as a function of probe delay at different grating periods is shown below:

After sample excitation, the transient grating begins to decay as a result of charge carrier diffusion and recombination. The diffracted probe intensity begins to decrease. The rate of signal decay depends on the period of the induced transient grating. If the period is small, that means that the diffraction grating is fine. Hence, the charge carrier diffusion will dissipate the fine grating faster. If the grating is coarse, it is less sensitive to diffusion and is able to diffract the probing pulse for longer. By plotting the diffraction signal on a semi-logarithmic scale, diffraction grating time τ_G can be calculated using linear fitting:

$$\eta \propto \exp\left(-\frac{2t}{\tau_G}\right), \tag{7}$$

where η is the diffraction signal, that is decaying with an exponential function of τ_G.

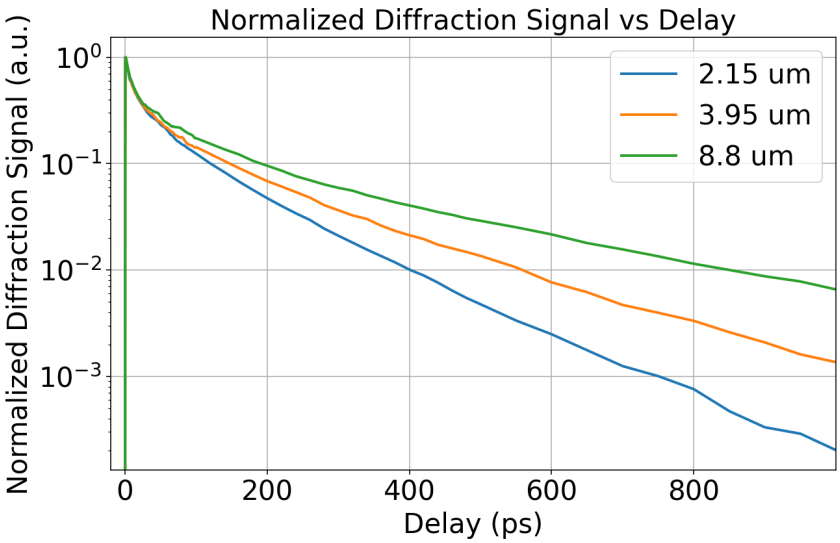

Figure 12: Example of diffracted probe decay kinetics of UID MOVPE-grown GaN sample measured at different grating periods at 120 $\frac{\mu J}{cm^2}$ excitation fluence.

The observed decay is due to the relaxation or dissipation of the excited charge carriers:

$$\frac{1}{\tau_G} = \frac{1}{\tau_R} + \frac{1}{\tau_D} = \frac{1}{\tau_R} + \frac{4\pi^2 D_a}{\Lambda^2}, \tag{8}$$

where τ_G is the grating time, acquired from linearly fitting the probe diffraction kinetics, τ_D is the grating decay time constant due to diffusion of charge carriers, and τ_R is the charge carrier recombination time.

By plotting the τ_G values against different grating periods and linearly fitting the resulting dependence (example shown in Figure 13), τ_R is obtained, which is the inverse of the intercept. Ambipolar diffusion coefficient D_a is then extracted as the slope of this function.

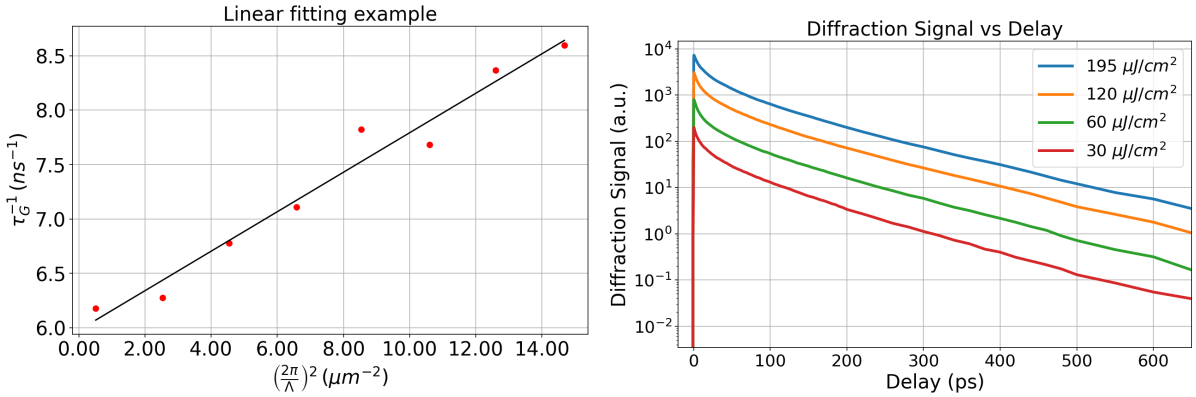

Figure 13: Example of ambipolar diffusion constant calculation for UID MOVPE-grown GaN sample, under the excitation of 120 $\frac{\mu J}{cm^2}$ at varying transient grating periods. As well as an example of diffracted probe decay kinetics of GaN measured at different fluences.

4.3 Photoluminescence Measurement

In this section time-integrated photoluminescence (TIPL) measurement setup and its relevant technical parameters as well as the theoretical background for relative quantum efficiency estimation are presented.

4.3.1 Measurement Setup

All samples were excited using a femtosecond laser (Carbide by *Light Conversion*), operating at a central wavelength of 1030 nm, with a pulse duration of approximately 200 fs. The laser was run at an average power of 40 W with 100 kHz repetition rate, corresponding to 400 μJ energy pulses.

Since 1030 nm wavelength falls well into the transparency window of GaN, the photon energy is insufficient to effectively generate electron-hole pairs in the material. Therefore, the excitation wavelength was converted to the ultraviolet by i-OPA (an industrial, direct-mounted optical parametric amplifier by *Light Conversion*). It utilizes multi-stage parametric amplification process in BBO crystals, as well as second harmonic generation of signal and idler to provide a wide, tunable wavelength selection range. Since the bandgap of GaN is 3.4 eV, UV wavelengths are required for successful excitation of the material. For this reason 340 nm wavelength was used (a second harmonic of 680 nm signal). Wavelength conversion from 1030 nm to 340 nm provides photons with energies above the bandgap of GaN. The latter wavelength was used to excite all the samples in this study.

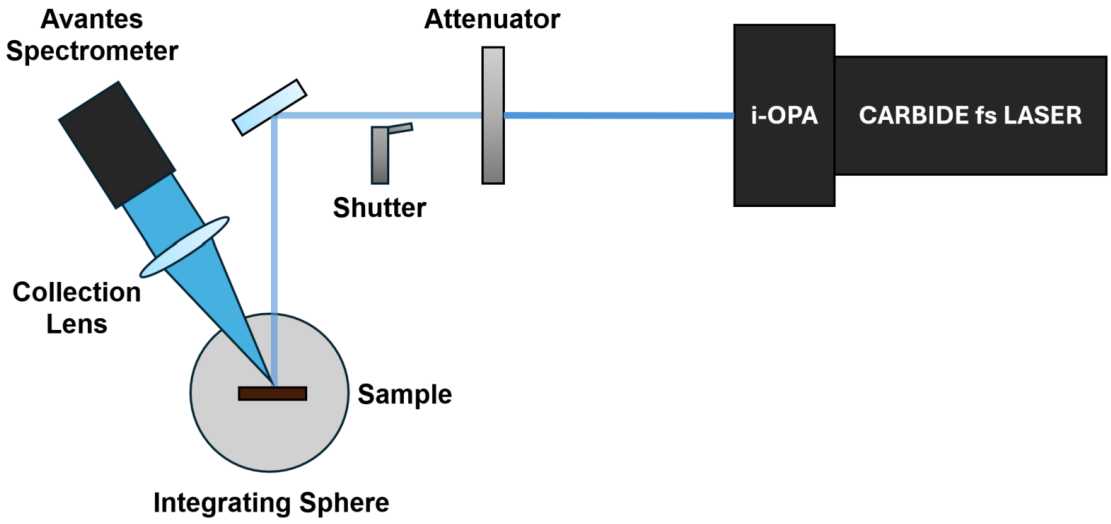

Figure 14: Photoluminescence measurement setup used to record PL spectra with the spectrometer outside the integrating sphere. These measurements provide relative PL spectra for all samples. To obtain an absolute reference, several samples were additionally measured with the spectrometer coupled directly to the integrating sphere. The absolute integrated PL from these reference measurements was then used to scale the relative integrated PL curves of all samples to quantitative values.

The excitation fluence (supplied energy per area) on the sample was controlled using an attenuator placed after the harmonic generation stage (Figure 14). As an attenuator, a variable neutral density filter was used. It was implemented as a glass disk, coated with varying thicknesses of aluminum. It provides attenuation in the UV-VIS-NIR range due to suitable reflectivity characteristics of aluminum. This approach allowed the pulse energy to be reduced while keeping the beam diameter (and thus the illuminated area on the sample) constant. For each attenuator setting, the corresponding excitation level (fluence) was recorded and used as the experimental parameter for excitation-dependent PL measurements.

An integrating sphere (Figure 14) was used to account for the randomness of directionality of the emitted photoluminescence and enable reliable comparison between the samples. The integrating sphere provides spatially uniform light via multiple diffuse reflections so that the detected signal more closely represents the total photon flux emitted by the sample. This is particularly important for quantitative comparison between differently irradiated epitaxial GaN layers, where differences in absorption, surface quality and re-emission geometry can influence observed the PL emission intensity.

The integrating sphere output was coupled to an Avantes spectrometer using an optical fiber (Figure 14). The spectrometer recorded the full PL spectrum for each excitation condition. To ensure that the measurements and excitation levels are consistent across samples, spectra were acquired using fixed acquisition settings where possible, while avoiding the saturation of the detector. In addition, dark spectra (with the excitation blocked via an external, electrically controlled shutter) were recorded and subtracted to remove detector background and ambient light contributions. Where necessary, the integration time was adjusted in a controlled manner and the measured spectra were normalized accordingly to retain quantitative comparability between measurements. Spectral correction was performed by dividing the measured PL spectra by the wavelength dependent spectral response (responsivity) of the detection system, thereby compensating for its non-uniform sensitivity.

All samples were first measured using the external collection geometry shown in Figure 14, where the emitted PL was collected by a lens and directed to the spectrometer. This configuration was used to acquire excitation-dependent PL spectra consistently across the full sample set. However, it only provides the relative emission because the detected signal depends on collection efficiency and alignment. To establish a quantitative reference for the emitted photon flux, one representative sample was additionally measured with the spectrometer coupled to the integrating sphere. Inside the sphere, the detected signal is proportional to the total emitted photoluminescence. The integrated PL obtained from this in-sphere measurement was treated as an absolute reference. The excitation-dependent integrated PL curves of all samples, measured in the external geometry, were then scaled by a single multiplication factor so that the corresponding curve of the reference sample

matched its integrating-sphere value.

Overall, the setup shown in Figure 14 enabled excitation-dependent PL spectroscopy at a fixed temperature with collection of the total emitted luminescence. The use of UV excitation, attenuation of the incident fluence, and integrating-sphere collection provides the means for the comparison of the emission strength between differently irradiated AT-MOVPE-GaN samples and for evaluating the trends of relative QE.

4.3.2 QE Evaluation via Three Measurement Approach

The quantum efficiency (QE) is defined as the ratio of the number of emitted photons to the number of photons that were absorbed upon sample excitation. Unlike external quantum efficiency, which is calculated relative to the number of incident photons, QE is calculated relative to the number of absorbed photons. Therefore, it excludes losses caused by incomplete absorption and better represents the intrinsic emission efficiency of the material. In this work, QE was evaluated using an integrating sphere. The "three measurement approach" method was used. It was originally introduced by *de Mello et. al.* and later discussed in great detail with rigorous theoretical treatment by *Leyre et. al* [32].

An integrating sphere is well suited for measuring QE. It enables a homogenized collection of photoluminescence emitted by the sample towards all directions. Meaning that the relative distribution of every emitted spectral component is homogenized inside the sphere. In this way the sensitivity to the directionality of the emission, sample scattering and the alignment of the collection optics is minimized.

The three-measurement approach separates the detected spectrum into two wavelength regions:

- Excitation region - around the incident excitation wavelength. When no sample is present in the sphere, the detected signal should only appear in the excitation region. It will be called the "L-region".

- Emission region - when a sample is present in the integrating sphere, emitted PL bands will appear in the emission region. It is assumed that the emission region does not overlap with the excitation region. If it did, additional corrections are necessary to account for that. It will be called the "P-region".

Because the QE calculation compares photon counts at different wavelengths, the measured spectra must be corrected for the wavelength-dependent response of the detection system. After the spectral correction, the obtained spectrum is proportional to the radiant flux in the sphere. Consequently, this means that all the arithmetic calculations done to obtain the quantities explained below are performed on spectra that have been corrected for the systems spectral response.

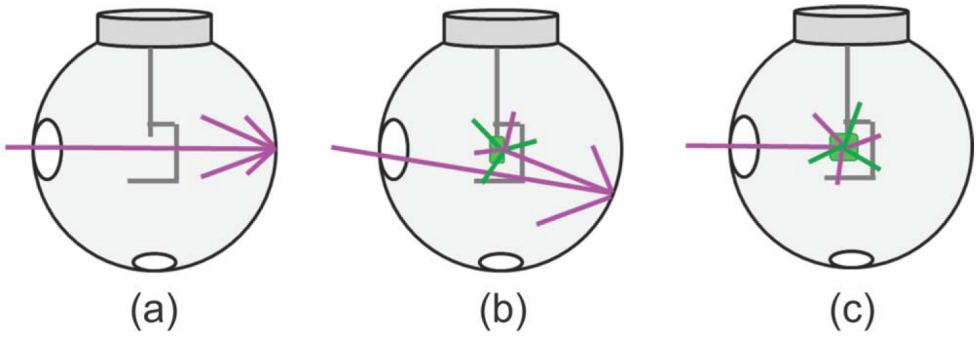

Figure 15: The geometry of each of the PL measurement with an integrating sphere [32]. Measurement A, B, and C correspond to a), b) and c) depicted geometries accordingly.

In the three measurement approach method, three measurements are carried out in the integrating spheres geometries shown in Figure 15.

- Measurement A - sample outside of the sphere.
- Measurement B - sample inside the sphere, turned out of the laser beams way.
- Measurement C - sample inside the sphere, directly illuminated by the excitation laser beam.

Each of the measurements obtain certain information about the absorption and photoluminescence of the sample:

- Measurement A:
  - L_a - number of photons detected in the excitation region.
- Measurement B:
  - L_b - number of photons detected in the excitation region, reduced due to indirect absorption of the sample inside the sphere, out of the way of direct laser beam.
  - P_b - number of emitted photons detected in the emission region due to indirect excitation of the sample.
- Measurement C:
  - L_c - number of photons detected in the excitation region (further reduced due to direct absorption of the excitation beam by the sample).
  - P_c - number of emitted photons detected in the emission region due to direct and indirect excitation of the sample.

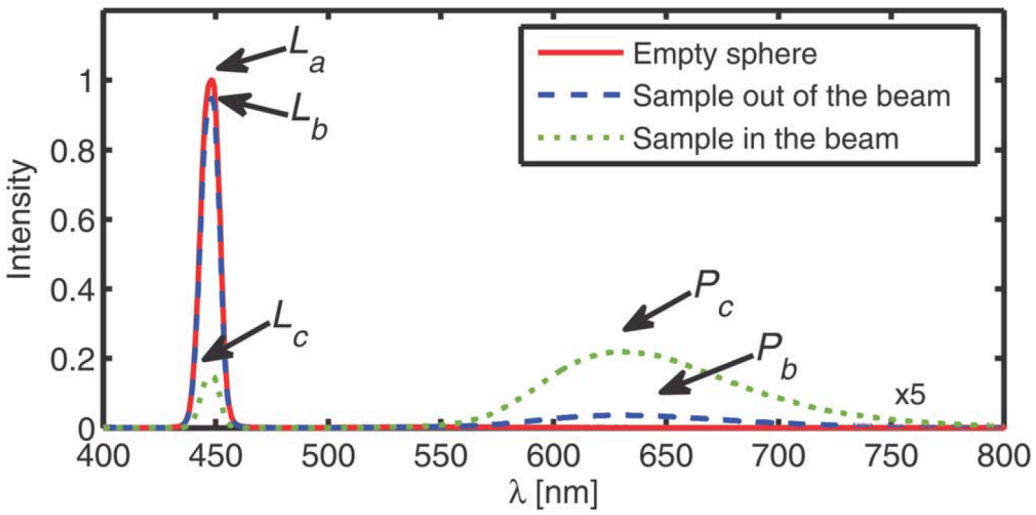

Figure 16: Typically observed PL spectra with three measurement approach. Corresponding spectral regions are denoted as discussed previously. [32].

The latter regions are well illustrated in Figure 16, the example of usual PL spectra obtained via three measurement approach:

In the empty integrating sphere, measurement (red line), only the excitation line is observed, and its integrated signal defines L_a. When the sample is placed inside the sphere but moved out of the direct beam (blue dashed line), the excitation line is slightly reduced due to indirect absorption of diffusely reflected light within the sphere, giving L_b, and a weak photoluminescence band becomes visible, corresponding to P_b. This is observed because even due to indirect excitation, the sample can generate PL emission. When the sample is positioned in the direct excitation beam (green dotted line), the excitation line is reduced much more strongly, yielding L_c, while the increased emission band, defines P_c as the PL generated by both direct and indirect excitation. So, the three measurement approach quantifies and accounts for the background PL emission, caused by indirect excitation of the sample inside the sphere.

The key step when evaluating QE, is determining the direct absorption of the sample, at the excitation wavelength. In the three measurement approach, direct absorption A_{dir} is calculated from the excitation band integrals as follows:

$$A_{\mathrm{dir}} = 1 - \frac{L_c}{L_b}. \tag{9}$$

The QE can then be calculated as:

$$QE = \frac{P_c - (1 - A_{\mathrm{dir}})\, P_b}{L_a\, A_{\mathrm{dir}}}. \tag{10}$$

Physically, the denominator of eq. (10) represents the number of absorbed excitation photons. The numerator corrects the measured PL emission P_c by subtracting the part of

the emission that is attributed to indirect excitation due to the scattering inside the sphere. P_b quantifies the emission generated when sample is not illuminated directly. Finally, the factor $1 - (A_{dir})$ accounts for the fraction of light that remains available for indirect excitation when the sample is inside the beam.

4.3.3 Relative QE Evaluation

The full three measurement integrating sphere technique described above provides an absolute QE without requiring an external reference sample. In this work, the complete three measurement approach was performed for several samples in order to obtain a quantitative emission efficiency etalon. Only mildly irradiated samples showed enough photoluminescence intensity to be reliably measured inside the sphere, without saturation due to excitation laser line. The remaining samples were measured using the external collection geometry, which yields excitation-dependent PL spectra that are internally consistent within the same optical configuration but do not directly provide absolute emitted photon numbers of each sample. To correlate the remaining samples with the absolute values of etalon samples, the following technique was used:

1. All samples were measured collecting the photoluminescence outside of the sphere, using the geometry presented in Figure 14.

2. Spectral correction was performed to account for wavelength sensitivity of the detection system.

3. Using the integrating sphere measurements of the reference samples L_a, L_b, L_c, P_b, P_c were obtained by integrating the spectrally corrected data over the corresponding emission and excitation regions. QE and A_{dir} were calculated.

4. For each measured sample in the external collection geometry, the PL spectrum was integrated over the emission region P to obtain an excitation dependent quantity that is proportional to the amount of emitted photons. As all the collection optics and alignment was constant for all measured samples, this obtained quantity provides a constant relative measure of emission between the samples.

5. A multiplication factor C was obtained when comparing the emission of the reference samples inside the integrating sphere, and using the outside detection geometry at a single excitation. This scaling factor was then applied to all externally measured samples so that their integrated PL curves are expressed on the same absolute scale as the integrating sphere reference.

5 Results and Discussion

In this section, the results are presented. Ambipolar diffusion coefficients, carrier lifetimes and diffusion lengths of the sample set, provided by LITG measurements, are shown. Carrier recombination pathways, probed via PL measurements are presented. QE values are determined and compared for all samples.

5.1 Carrier Dynamics

LITG measurements show how fast the photo-generated charge carriers are able to move in the sample. Ambipolar diffusion coefficient describes the rate at which the carriers dissipate photo-excitation grating due to the created gradient. While carrier lifetime denotes the duration of generated charge carriers diffusion. The ambipolar diffusion coefficient is heavily influenced by the charge carrier mobility in the sample, while the carrier lifetime is governed mainly by the density of defects.

5.1.1 Ambipolar Diffusion

Using the measured LITG grating decay kinetics and by fitting eq. (8), the ambipolar diffusion coefficient and how it depends on photo-generated carrier densities (excitation fluence) in all irradiated samples was calculated. The results are shown in Figure 17.

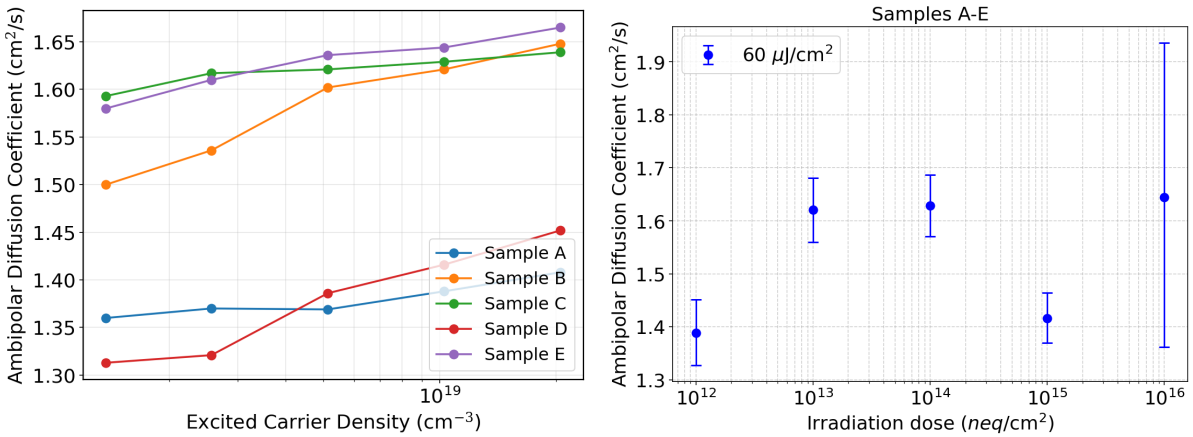

Figure 17: Measured photo-generated charge carrier ambipolar diffusion coefficients of all irradiated samples at different photo-generated carrier densities (left). Different samples are denoted as different colors, least through most irradiated in an alphabetical order. The ambipolar diffusion coefficient could not be determined in an accurate way for Sample F - the most heavily irradiated GaN. The ambipolar diffusion coefficient dependence on irradiation dose with error bars (right).

Analyzing Figure 17, one can infer that the ambipolar diffusion coefficient does not depend on the dose of irradiation that AT-MOVPE-GaN samples have received. As the ambipolar diffusion coefficient is primarily influenced by the charge carrier mobility, one

can deduce that it is not significantly influenced by the irradiation process. As all samples come from a single growth process, carrier mobility thus is expected to be similar if unaffected by the irradiation. It must also be noted that the carrier diffusion depends on the extent of scattering, recombination and trapping effects. However, LITG results show that introducing excess point defects to the lattice of GaN does not introduce sufficient scattering and trapping effects to meaningfully change the carrier diffusion rates in the material.

Furthermore, Figure 17 shows that ambipolar diffusion coefficients increase across all samples with increasing excitation fluence (excited carrier densities). Although the literature reports that such increase of ambipolar diffusion coefficient at higher photo-generated carrier densities can be related to degenerate carrier plasma effects, where carriers no longer follow purely classical Boltzmann statistics and force additional carriers into higher-energy states, carrier densities used in this work are insufficient for this mechanism to take place [33]. Rather we believe that the observed dependence is more likely to be related to the transition of different ambipolar diffusion regimes. At low excitation, the ambipolar diffusion coefficient is strongly influenced by the equilibrium carrier population. Since the investigated samples are of UID n-type, the minority carriers are holes, the concentration of which at equilibrium is small compared to electrons. So, even though electrons diffuse faster, they cannot separate far from holes in order to maintain charge neutrality. Therefore minority carriers - holes - become the limiting factor, as the electron-hole pairs move with rates closer to the motion rates of holes. This can be mathematically obtained from eq (2).

In the low-injection regime of UID n-type GaN, we can assume:

$$n_0 \gg p_0, \qquad n_{\text{ex}} \ll n_0. \tag{11}$$

Approximating the numerator and denominator of eq. (2) as:

$$\text{Numerator:} \quad n_0 + p_0 + 2n_{\text{ex}} \approx n_0, \tag{12}$$

$$\text{Denominator:} \quad \frac{n_0 + n_{\text{ex}}}{D_h} + \frac{p_0 + n_{\text{ex}}}{D_e} \approx \frac{n_0}{D_h}. \tag{13}$$

Therefore,

$$D_a \approx \frac{n_0}{\frac{n_0}{D_h}} = D_h. \tag{14}$$

Since similar dependence is observed in all samples, it shows that it is an intrinsic property of GaN and is not an effect of irradiation.

5.1.2 Carrier Lifetime

The carrier lifetimes, provided by LITG measurements, are depicted in Figure 18 and listed in Table 4. This time a clear irradiation influence is visible. A reduction in carrier lifetime is observed in more heavily irradiated GaN samples (right plot in Figure 18, magnitudes of reduction listed in Table 5). Samples A-C show little reduction in carrier lifetimes compared to Samples D-F. Meaning that only irradiation doses of 10^{15} $\frac{neq}{cm^2}$ and above start inducing sufficient point defects into the lattice of AT-MOVPE-GaN (as described in the literature review sections) to result in moderate reduction of carrier lifetime (see the right plot in Figure 18). Generated defects act as non-radiative recombination sites. They provide additional pathways for electron-hole pairs to recombine compared to samples with smaller irradiation doses.

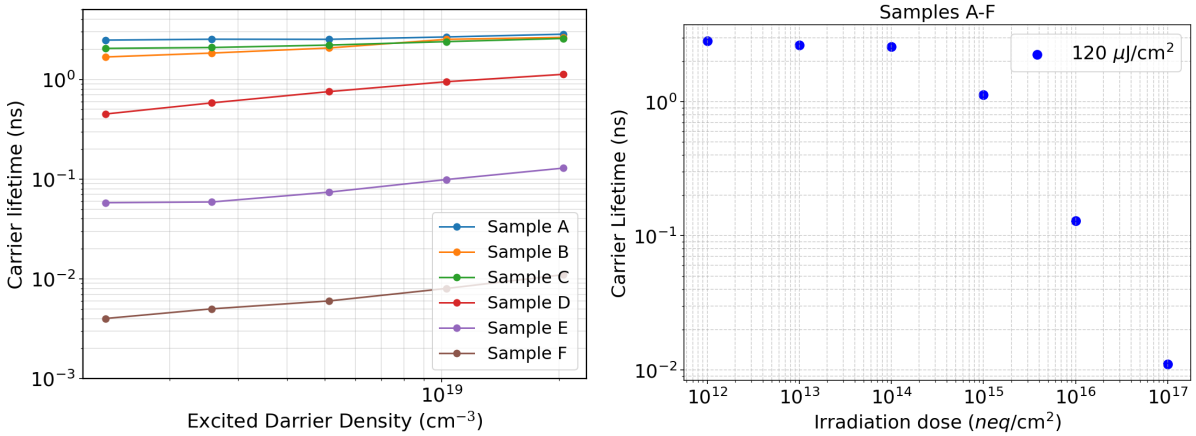

Figure 18: Measured photo-generated charge carrier lifetimes of all irradiated samples at different excitation fluences (on the left). Measured photo-generated charge carrier lifetimes of all irradiated samples with different neq doses, at 120 $\frac{\mu J}{cm^2}$ excitation fluence (on the right).

Table 4: Carrier lifetimes of Samples A–F at different excitation fluences. In heavily irradiated samples, the uncertainty of carrier lifetime calculations is greater.

Carrier Lifetimes (ns)					
Fluence (μJ/cm^2)	**8**	**15**	**30**	**60**	**120**
Sample A	2.5	2.5	2.5	2.7	2.8
Sample B	1.7	1.8	2.1	2.5	2.6
Sample C	2.0	2.1	2.2	2.4	2.6
Sample D	0.5	0.6	0.8	0.9	1.1
Sample E ≈	0.058	0.059	0.074	0.099	0.129
Sample F ≈	0.004	0.005	0.006	0.008	0.011

Table 5: Carrier lifetimes at the lowest and highest excitation fluences for Samples A–F.

Sample	**8 μJ/cm^2**		**120 μJ/cm^2**
Sample A	2.5 ns	$\leftarrow$	2.8 ns
Sample B	1.7 ns	$\leftarrow$	2.6 ns
Sample C	2.0 ns	$\leftarrow$	2.6 ns
Sample D	0.5 ns	$\leftarrow$	1.1 ns
Sample E $\approx$	0.058 ns	$\leftarrow$	0.129 ns
Sample F $\approx$	0.004 ns	$\leftarrow$	0.011 ns

Figure 18 (left plot) also shows that carrier lifetime generally increases at greater photo-generated charge carrier density. This behavior can be attributed to saturation of defect-related trapping centers. In the low-injection regime, the latter states are empty and are efficient at capturing photo-generated charge carriers. However, as their density increases, the previously empty states become more and more filled. Thus the SRH recombination efficiency is estimated to decrease (as later proven by PL measurements), and carrier lifetimes are expected to rise.

No clear systematic correlation is observed between the strength of saturation effects and irradiation dose. Thus we infer that irradiation process mainly affects the absolute value of carrier lifetime rather than its excitation-dependence. This suggests that higher irradiation doses increase the overall density of non-radiative recombination centers, but the fluence-dependent filling or saturation of these centers follows a similar trend across the sample set.

Even though earlier Figure 17 showed that the diffusion coefficient does not change with irradiation dose, however, now examining the carrier lifetime results one can see that the duration of the diffusion does. This means that charge carriers travel a shorter path (although just as fast) until a trap (a radiation-induced defect) is met (well-illustrated by Figure 19, showing the diffusion lengths of all samples, calculated using eq. (15)).

$$L_D = \sqrt{D_a \tau_R} \tag{15}$$

The obtained values of diffusion length are listed in Table 6. Since ambipolar diffusion coefficient could not be determined for Sample F, diffusion length was unable to be calculated for the sample with the heaviest irradiation dose.

Table 6: Carrier diffusion lengths of Samples A–E at 120 μJ/cm^2 excitation fluence. Sample F is excluded because the ambipolar diffusion coefficient could not be reliably determined.

Sample	**Irradiation dose** ($\frac{neq}{cm^2}$)	**Diffusion length** (μm)
Sample A	1×10^{12}	0.317
Sample B	1×10^{13}	0.330
Sample C	1×10^{14}	0.325
Sample D	1×10^{15}	0.202
Sample E	1×10^{16}	0.074

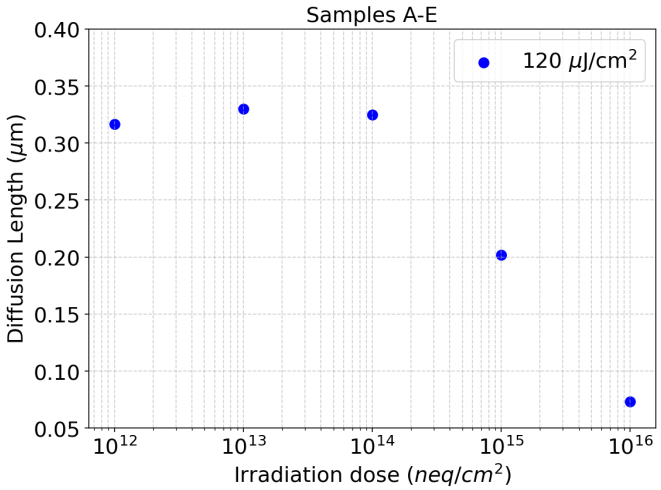

Figure 19: Measured photo-generated charge carrier diffusion lengths of all irradiated samples at 120 $\frac{\mu J}{cm^2}$ irradiation fluence, and their dependence on irradiation dose.

The calculated diffusion lengths show that Samples A–C have very similar carrier transport distances, remaining around 0.33-0.32 μm. This agrees with the observation made earlier, that mild to moderate irradiation does not strongly affect the ambipolar diffusion coefficient or the carrier lifetime. A clear reduction appears for Sample D, where the diffusion length decreases to 0.20 μm, and becomes even stronger for Sample E, reaching only 0.08 μm. Since the diffusion coefficient itself remains relatively unchanged, this reduction is mainly caused by the shortening of carrier lifetime due to irradiation-induced non-radiative recombination centers. Thus, at higher irradiation doses, carriers do not diffuse more slowly, but they recombine much sooner, resulting in a shorter diffusion length.

5.1.3 Hysteresis of LITG Measurements

During LITG measurements, a hysteresis in the measured grating decay kinetics was observed in more heavily irradiated samples D and F (depicted in Figure 20). During the second measurement in the same spot on the sample, a clear reduction of photo-excited carrier decay rate is observed. These effects were explored in detail and attributed to a combination of local thermal defect annealing due to intense fluence of the pumping laser beam as well as recombination-enhanced defect reaction effects.

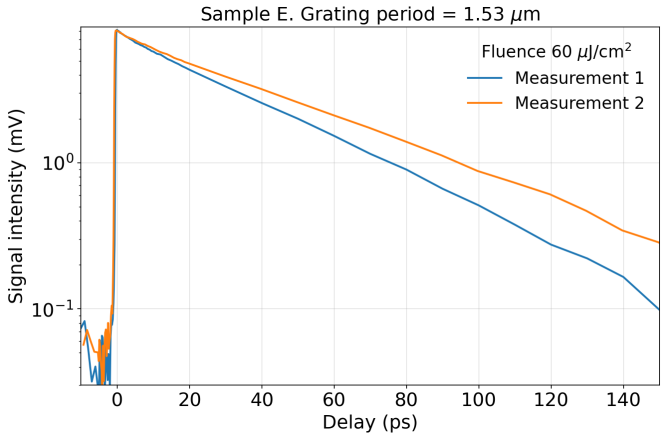

Figure 20: Observed hysteresis of LITG kinetics in Sample E, Low-High-Low excitation fluence sequence. Both measurements were carried out at 60 $\frac{\mu J}{cm^2}$ excitation fluence, 1.53 μm grating period.

Single sample was measured several times - starting from 8 $\frac{\mu J}{cm^2}$ (low excitation), increasing it to 120 $\frac{\mu J}{cm^2}$ and reducing it back down to 8 $\frac{\mu J}{cm^2}$ in one uninterrupted measurement sequence. To determine whether the observed effect was caused by the probe beam, the measurement sequence was then reversed. The same sample was also measured starting from 120 $\frac{\mu J}{cm^2}$ (high excitation), reducing it to 8 $\frac{\mu J}{cm^2}$, and again increasing it back to 120 $\frac{\mu J}{cm^2}$. The main idea being that if this effect is coming from the probing beam, no difference would be observed when measuring the sample in High-Low-High or Low-High-Low excitation fluence sequence, as the intensity of the probe is constant throughout the entire measurement. On the other hand, if the pumping beam is responsible for the observed hysteresis in the measurements, it would be apparent in Low-High-Low excitation sequence, and not in High-Low-High (as the sample would be immediately annealed at the starting 120 $\frac{\mu J}{cm^2}$ pumping fluence). Both excitation sequences are depicted in Figure 21.

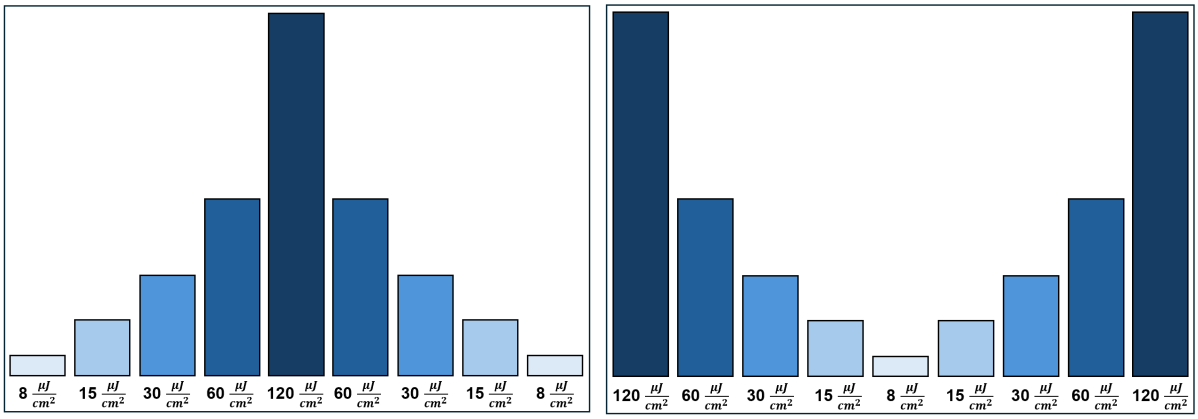

Figure 21: Low-High-Low excitation sequence (on the left), and High-Low-High (on the right).

Carrier lifetimes were used as an indicator of defect heating-annealing effects. Since only two most heavily irradiated samples (with irradiation doses from 10^{16} $\frac{neq}{cm^2}$) showed LITG hysteresis effects, they were measured 4 times each, in the excitation fluence sequences, described beforehand. Carrier lifetime is suspected to increase due to the defect annealing effects (as one can observe in the slower decaying LITG kinetics in Figure 20). Figure 22 depicts how laser-beam-induced defect annealing affects the carrier lifetimes.

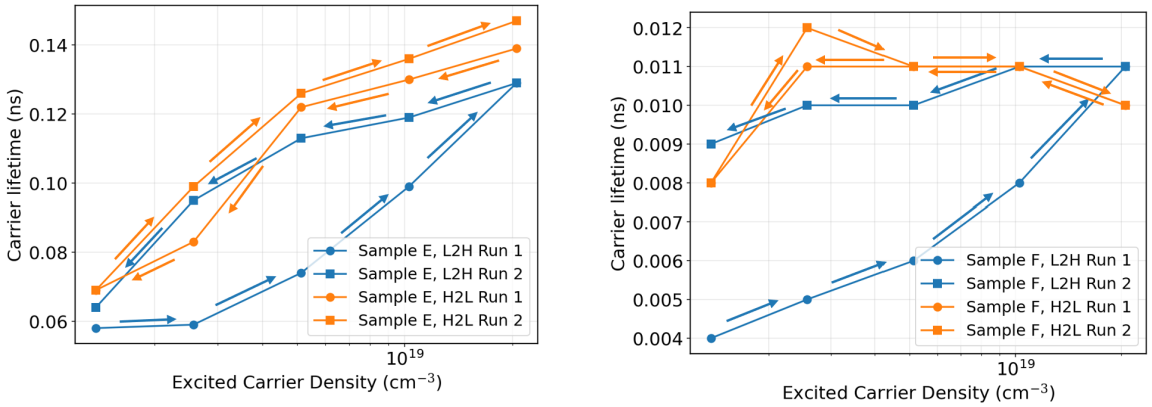

Figure 22: Carrier lifetime dependences on excitation fluence for two most heavily irradiated AT-MOVPE-GaN samples. L2H and H2L denotes Low-High-Low and High-Low-High excitation sequences respectively. Most intuitively, Low-High-Low plots are to be read from lowest excitation starting with "Run 1" to the highest, and back, along "Run 2" line. High-Low-High sequence is read *vice versa*. Color-matched arrows indicate the excitation sequence.

Figure 22 shows that there is a clear carrier lifetime increase in the measurements, utilizing the Low-High-Low excitation sequence. Therefore, we deduce that indeed the pumping beam is responsible for the hysteresis effects. No significant change in carrier lifetime was observed in High-Low-High excitation sequence. Meaning that since the first measurement is already carried out at 120 $\frac{\mu J}{cm^2}$ of fluence, the sample is immediately

annealed, carrier lifetimes are increased, and thus the hysteresis effects are no longer present.

We speculate, although the pump laser beam is focused into the sample, it should not be sufficient to reach the required temperatures (approximately 600 K) to fully mobilize the present N and Ga interstitials in the material, allowing them to redistribute, filling the abundance of vacancies [34]. Which would be a plausible mechanism for improving the crystalline quality of the material, thus increasing the carrier lifetime. However, another plausible mechanism, observed in group III-nitrides is the so-called recombination-enhanced defect reactions (REDR) [35].

REDR refers to defect migration or transformation driven by the vibrational energy released during non-radiative recombination of excess carriers, rather than by ordinary bulk heating alone. Photo-excited carriers recombine through defect-related non-radiative centers. Subsequently they release energy that can in turn locally stimulate defect diffusion, annihilation, reconfiguration, dissociation and in some cases generation. There are two types of REDR events: "thermal spike" - in which the recombination energy is locally distributed as a confined heating-annealing event, and a "phonon kick" - in which the energy is directed along a specific defect reaction coordinate, it enables atom migration that would not conventionally occur during thermal annealing. These effects normally produce a hysteresis-like response - where a prior high-fluence exposure affects the results of the following low-fluence measurement. REDR mechanism is especially relevant in nitrides, where V_{Ga}-related centers have been proposed as possible "carrier killer centers" that are capable of driving the local defect reactions through the energy, released during recombination process [35]. Hence we believe that the observed increase in carrier lifetime after high-fluence exposure in heavily irradiated AT-MOVPE GaN is a combination of both local annealing and REDR effects.

Although the hysteresis effect was clearly visible from the carrier lifetime values, the same analysis could not be applied reliably to the ambipolar diffusion coefficient. Since this effect was present in heavily irradiated samples, ambipolar diffusion coefficients retrieval uncertainty was too high (see Figure 17). For Sample F, the ambipolar diffusion coefficient was not reliably calculated at all. Therefore, carrier lifetime was used as the main indicator of the hysteresis effect, while possible changes in ambipolar diffusion during the measurement sequence will not be discussed quantitatively.

5.2 Carrier Recombination

This section presents the results of carrier recombination analysis via time-integrated photoluminescence measurements. The main PL lines visible in the spectra and their dependence on excitation fluence are explored in detail. Quantum efficiencies were evaluated highlighting the effects of irradiation on radiative recombination.

5.2.1 Excitation-dependent Photoluminescence

Firstly, all irradiated AT-MOVPE-GaN samples were measured "outside" of the sphere. Meaning that the spectrometer was placed behind the collection lens (as shown in Figure 14). This provides the general dependence of PL emission efficiency on excitation fluence (or photo-generated carrier density) in arbitrary registered PL intensity units. The results are depicted in Figure 23.

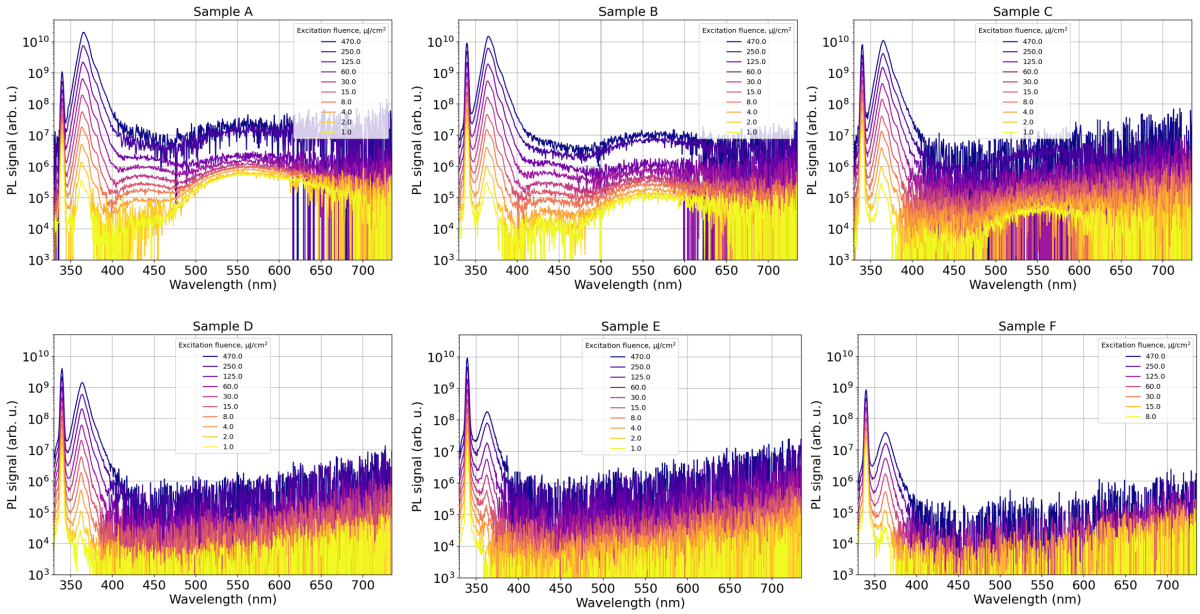

Figure 23: Photoluminescence spectra of all samples, measured via an integrating sphere, with spectrometer outside of the sphere, behind the collection lens.

There are four distinct regions to be observed in the measured spectra:

- **(340 nm)** Laser excitation line. It corresponds to the wavelength used to excite the samples and induce carrier recombination processes; it originates from the unabsorbed and scattered light. Which later was collected by the lens and the spectrometer. Since the same excitation wavelength was used for all samples, it is consistent throughout all of the measured PL spectra. It is treated as an artifact of the experiment and not material-related emission band.

- **(365 nm)** Recombination through the near-band-edge transitions. It corresponds to 3.4 eV, which is the well-known characteristic figure of GaN - the bandgap of the material. Charge carriers radiatively recombine via band-to-band transition, emitting photons of the corresponding energy to the bandgap. Its intensity usually directly corresponds to the efficiency of radiative recombination in the material.

- **(400-460 nm)** The so-called blue luminescence (BL) band of GaN. It corresponds to 3.3-2.7 eV. It arises due to hydrogen-carbon defect complexes - either $C_N O_N - H_i$ or $C_N - H_i$. The abundance of the latter in MOVPE GaN grown on AT GaN substrates are well-known. They create defect levels that are close to the valence band. However, with energy supplied to the material these complexes are able to dissociate and leave $C_N O_N$ or C_N and H_i [36]. The latter impurities are able to participate in the yellow luminescence band.

- **(460-700 nm)** The so-called yellow luminescence (YL) band of GaN 2.7-1.8 eV, which extends into the blue luminescence line. In GaN it arises due to radiative recombination taking place between deep acceptor defects such as carbon-related centers C_N, gallium vacancy V_{Ga} complexes and impurity-vacancy centers involving hydrogen, oxygen, N_V, as well as Ga_i - all shallow donor-like defects. Such recombination process is known as the donor-acceptor pair (DAP) recombination process. Since incorporated donors and acceptors in the material comprise energy states, that are situated at varying distances from the valence and conduction bands, the emitted PL band is broad.

Further analyzing Figure 23, the effects of irradiation are clear and can be attributed to two main processes happening simultaneously:

- With increasing neutron-equivalent fluence, the YL, BL and main bands are all progressively quenched. Both YL and BL bands completely disappear in samples irradiated with 10^{15} $\frac{neq}{cm^2}$ dose. This is due to induced excess amount of displacement damage defects such as vacancies, interstitials and defect complexes. The latter radiation-induced defects primarily act as non-radiative SRH recombination centers rather than efficient emitters of PL. Meaning that as their density increases, they capture photo-generated carriers before they can radiatively recombine through near-band-edge or DAP channels. Effectively shifting the scales towards SRH recombination, thus it becoming the dominant mechanism. So, the quenching of PL in irradiated AT-MOVPE-GaN should be interpreted as the effect of non-radiative recombination dominance, rather than the removal or dissociation of yellow-emitting centers.

- Another plausible and important PL quenching mechanism is increased reabsorption of photoluminescence in irradiated samples. Although carriers radiatively recombine,

the emitted PL can be reabsorbed by the sample before escaping, thereby reducing the overall externally measured PL efficiency. This is due to appearance of new energy states within the bandgap. Irradiation process further increases the density of latter states. It generates V_N and V_{Ga}, as well as Ga_i and N_i, the latter can also form various complexes with pre-existing impurities in the material. All of them forming energy states at varying depths in the bandgap (listed in Table 7 and depicted in Figure 24).

Table 7: Irradiation-induced native point defect levels in GaN [37].

Defect	Type	Energy level
V_{Ga}	Acceptor	$\sim E_{\mathrm{V}} + 1.0$–$2.2$ eV
V_{N}	Donor	$\sim E_{\mathrm{C}} - 0.004$–$0.30$ eV
Ga_i	Donor	$\sim E_{\mathrm{C}} - 0.7$–$1.0$ eV
N_i	Acceptor	$\sim E_{\mathrm{C}} - 1.0$ eV

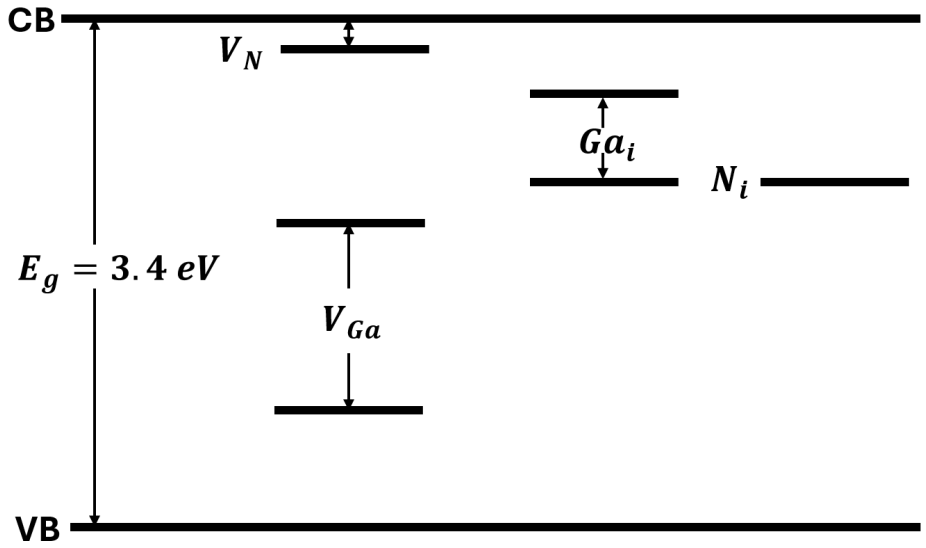

Figure 24: Energy band diagram of irradiation-induced point defect energy levels in GaN.

As a result, the material starts to absorb lower energy photons than its bandgap. YL PL band would be especially sensitive to this process as this absorption strongly overlaps with the latter region. Even if YL centers radiatively emit, a significant fraction of these photons end up reabsorbed by the sample. Its sequence of events are illustrated in Figure 25. Furthermore, the direct absorption factor A_{dir}, used in later evaluation of QE (see eq. (9) and eq. (10)), would not be affected by this process, as it was determined to be the same for all samples. It counters the possible case of absorption spectrum changes after excess point defect generation.

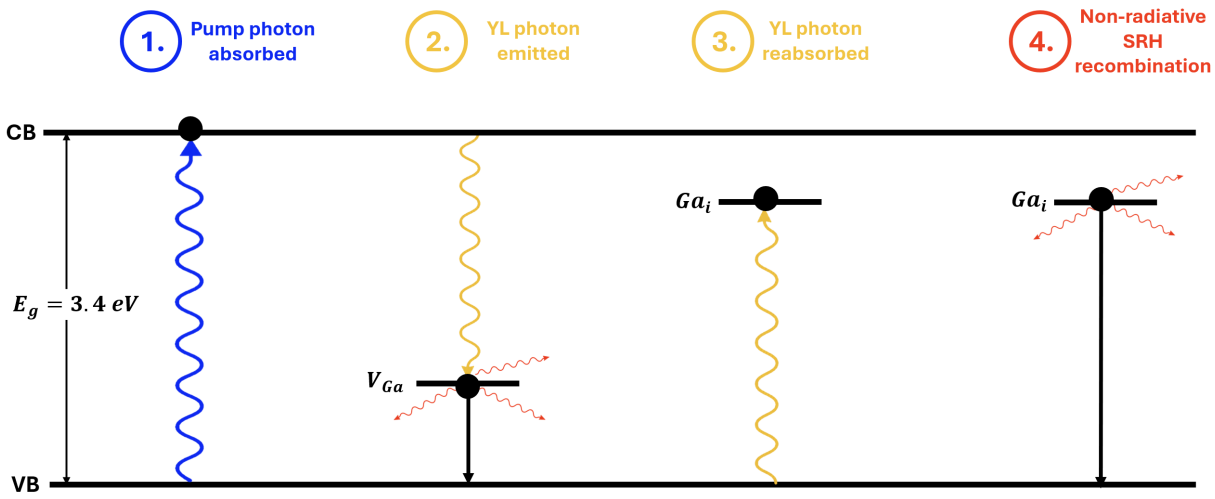

Figure 25: Reabsorption sequence of YL band in irradiated AT-MOVPE-GaN.

So, one can estimate that irradiation decreases both the internal (through SRH) and external (through reabsorption) quantum efficiencies of the sample.

Furthermore, the samples that were irradiated with heavier neutron doses look optically opaque at the macroscopic level (depicted in Figure 26). Further supporting the theory, that irradiated AT-MOVPE-GaN starts to absorb visible light (overlapping with YL band) due to point-defect-related energy states and consequently suppressing it via non-radiative SRH recombination.

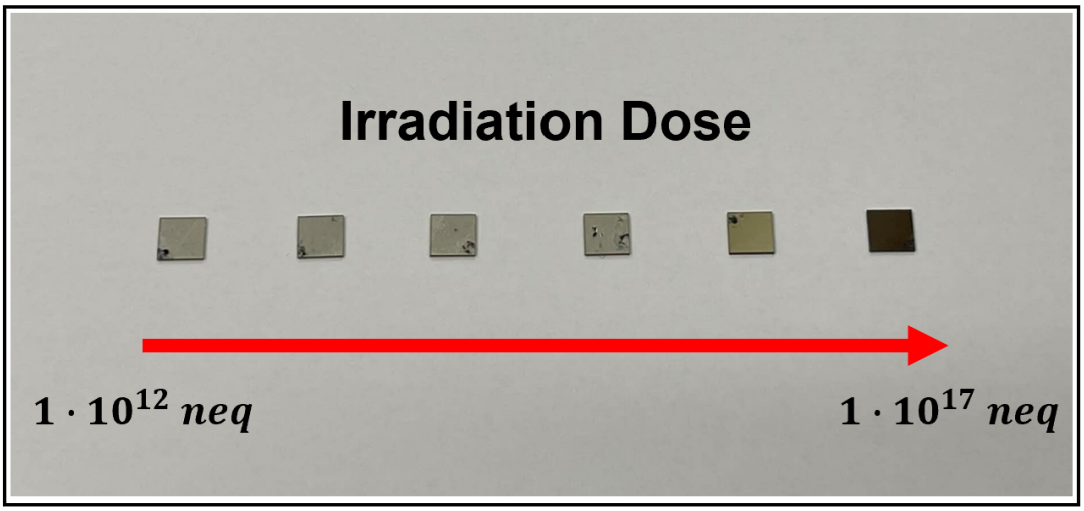

Figure 26: Picture of the investigated sample set. Mild to heavy irradiation in order: from left to right. Dark occasional blemishes visible on the samples are marker dots, indicating the growth direction, as well as burns from previously performed measurements. The latter sample locations were carefully avoided throughout this work during measurement setup alignment procedures.

5.2.2 Quantum Efficiency Evaluation

PL emission was measured inside the sphere for all samples (as previously discussed in methodology sections). The results are depicted in Figure 27. Since two of the most heavily irradiated samples did not show enough PL intensity inside the sphere before saturating the spectrometer with excitation laser line, their QEs were estimated via relative QE measurement method, described previously.

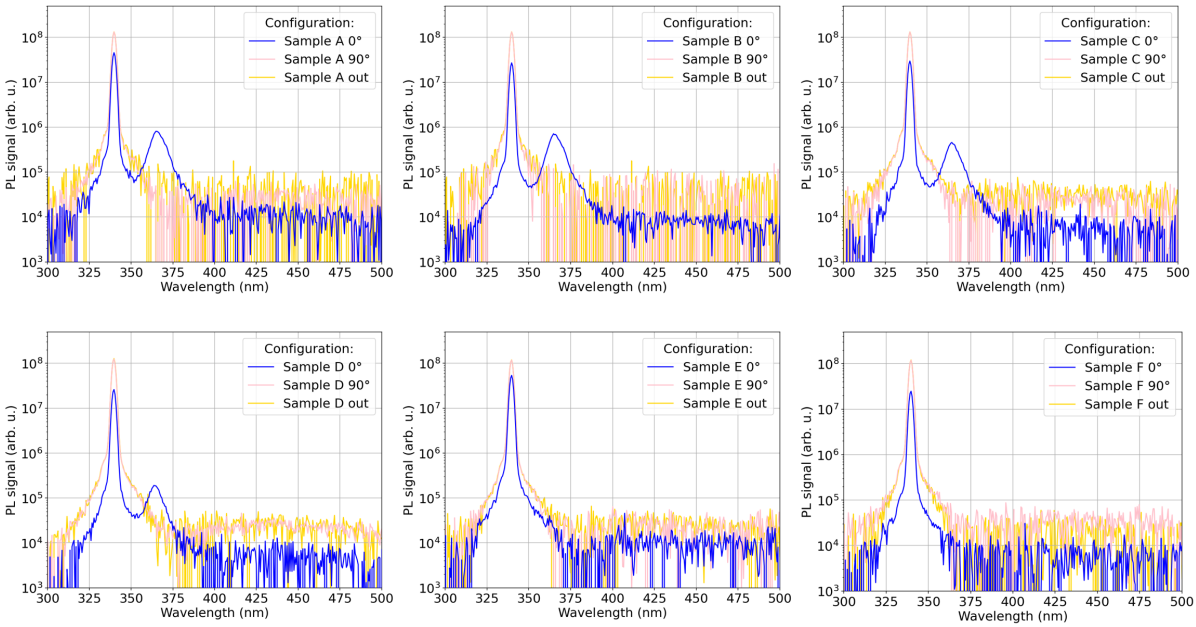

Figure 27: PL spectra of all irradiated samples, measured via collection of light inside the integrating sphere. The laser line was integrated from 330 to 345 nm, and GaN PL from 350 to 400 nm for PL QE calculations.

Figure 28 and Table 8 show the obtained PL quantum efficiencies of all irradiated samples. PL QE shows clear degradation with increasing irradiation dose. A fixed 125 $\frac{\mu J}{cm^2}$ fluence data cut shows that QE progressively decreases from Sample A to F, indicating that irradiation introduces additional non-radiative SRH pathways. This is consistent with excess point defect formation in the material as discussed previously. Furthermore, increased PL reabsorption effects due to abundance of sub-bandgap energy states (Figure 24) also reduce PL QE (through process previously depicted in Figure 25). These effects become especially apparent at heavy irradiation doses, reducing QE down to values, unable to be accurately measured via direct methods.

PL QE dependence on excitation fluence (left plot in Figure 28) suggests that increased charge carrier generation can overcome or even partially compensate the defect-induced non-radiative SRH via trap filling and saturation. At low excitation fluences, defect-assisted SRH recombination is dominant because many trap states are empty and can efficiently capture photo-generated carriers. As excitation fluence increases, these defect states become increasingly filled, while the probability of radiative band-to-band recombination

rises more strongly with carrier density (reported in the literature, via the use of ABC model [38]). Therefore, the relative contribution of radiative recombination increases and QE rises with excitation fluence. However, the latter compensation is not sufficient to recover the QE in heavily irradiated samples. Overall, the observed decrease in PL QE shows that irradiation-induced defect energy states enhance non-radiative SRH in the samples and allow it to dominate the competition over radiative near-band-edge recombination.

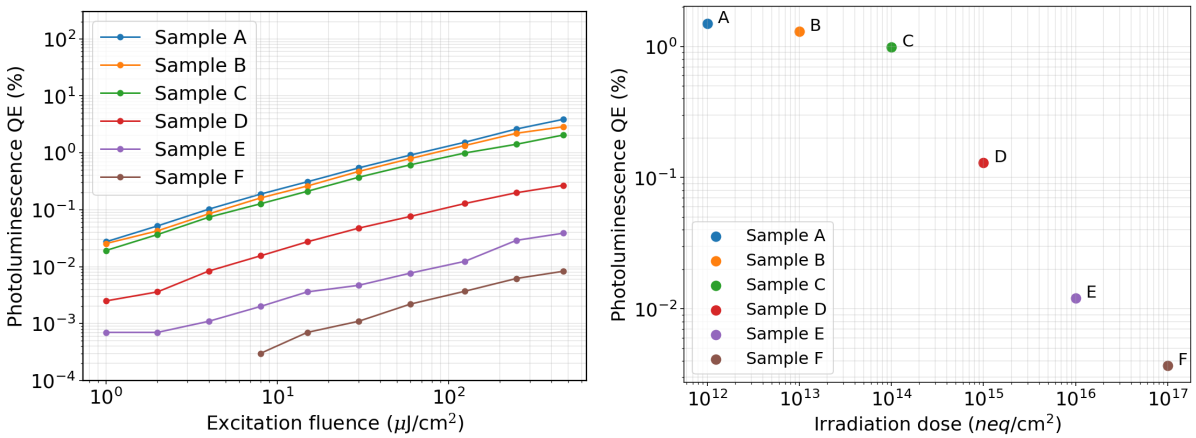

Figure 28: PL QE of all irradiated samples and its dependence on excitation fluence (on the left). PL QE at 125 $\frac{\mu J}{cm^2}$ excitation data cut, showing its dependence on irradiation dose (on the right).

Table 8: Photoluminescence quantum efficiency values of Samples A–F at different excitation fluences.

Photoluminescence Quantum Efficiency (%)										
Sample	**Excitation fluence (μJ/cm^2)**									
	1	**2**	**4**	**8**	**15**	**30**	**60**	**125**	**250**	**470**
A	0.027	0.052	0.10	0.19	0.31	0.54	0.91	1.5	2.6	3.9
B	0.025	0.043	0.085	0.16	0.26	0.47	0.79	1.3	2.2	2.9
C	0.019	0.037	0.074	0.13	0.21	0.37	0.61	0.99	1.4	2.1
D	0.0025	0.0036	0.0084	0.016	0.027	0.048	0.076	0.13	0.2	0.27
E	0.0007	0.0007	0.0011	0.002	0.0036	0.0047	0.0077	0.012	0.029	0.039
F	–	–	–	0.0003	0.0007	0.0011	0.0022	0.0037	0.0062	0.0083

The correlation observed in Figure 29, further supports that QE is linked to carrier recombination lifetime. Samples A-C, which have the lowest irradiation doses (resulting in longer carrier lifetimes) show the highest QE values. It indicates that the radiative recombination remains relatively efficient in mildly to moderately irradiated samples. In contrast, samples D-F shift towards lower QE and carrier lifetime values. It shows that irradiation-induced defects both shorten carrier survival time in the material as well as suppress photon emission. Therefore, the decrease of QE is consistent with the increasing dominance of non-radiative SRH recombination at higher irradiation doses.

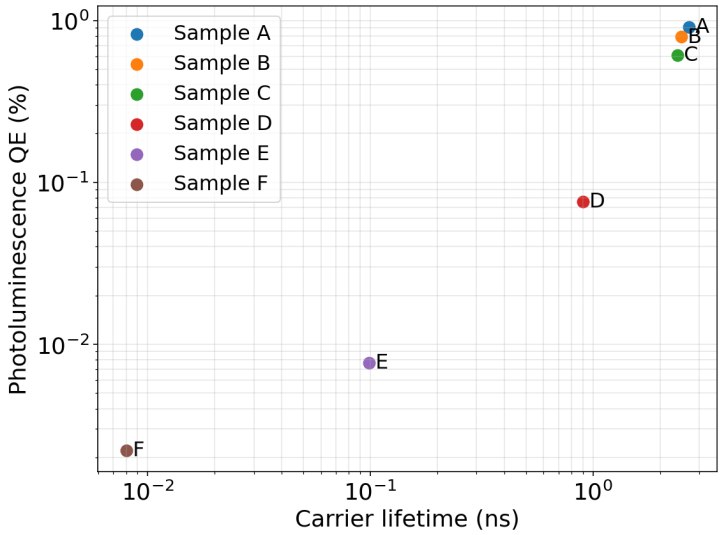

Figure 29: PL QE of all irradiated samples and its dependence on carrier lifetimes measured via LITG, at 60 $\frac{\mu J}{cm^2}$ excitation fluence.

6 Conclusions

- Neutron irradiation showed no significant effect on ambipolar diffusion in AT-MOVPE GaN. Indicating that carrier mobility remains unchanged.
- Carrier lifetime strongly decreases with irradiation doses upwards of $10^{15} \frac{neq}{cm^2}$ showing that induced point defects act as recombination-promoting, carrier trapping centers.
- A hysteresis effect of LITG measurements was observed for samples irradiated upwards of $10^{15} \frac{neq}{cm^2}$ after exposure to 120 $\frac{\mu J}{cm^2}$ fluence pump. Indicating that the results depend on prior optical excitation history. Possibly due to local defect annealing and recombination-enhanced defect reactions.
- PL measurements revealed progressive quenching effects of both near-band-edge and defect PL emission bands with increasing irradiation dose, resulting in QE drop. This was attributed to irradiation-induced point defects creating non-radiative SRH centers that compete with radiative recombination channels and induce sub-bandgap PL reabsorption losses.

7 Santrauka

Šiame darbe tiriama neutronų apšvitos įtaka krūvininkų dinamikai ir rekombinacijos procesams galio nitrido (GaN) epitaksiniuose sluoksniuose, užaugintuose ant amonoterminių GaN padėklų. Buvo analizuojama bandinių serija, apšvitinta skirtingomis neutronų dozėmis nuo 10^{12} iki $10^{17}\frac{neq}{cm^2}$. Krūvininkų pernašai įvertinti taikyta lazeriu indukuotų, dinaminių gardelių (angl. *"Laser-induced transient grating (LITG)"*) spektroskopija, leidžianti nustatyti ambipolinės difuzijos koeficientą bei krūvininkų gyvavimo trukmę. Rekombinacijos procesams bei kvantinio našumo pokyčiams tirti buvo pasitelktas laike integruotos fotoliuminescencijos spektroskopijos matavimo integruojančioje sferoje metodas. Gauti rezultatai parodė, kad neutronų apšvita ambipolinės difuzijos koeficientui reikšmingos įtakos neturi, tačiau stipriai mažina krūvininkų gyvavimo trukmę (ypač nuo $10^{15}\frac{neq}{cm^2}$). Tai rodo, kad apšvitinimo sukurti taškiniai defektai veikia kaip efektyvūs nespindulinės rekombinacijos centrai, tačiau reikšmingai nepakeičia krūvininkų judrio medžiagoje. Taip pat stipriai apšvitintuose bandiniuose pastebėtas ir LITG histerezės efektas, siejamas su vietiniu defektų iškaitinimu bei optiškai sukeltais defektų persitvarkymo procesais. Tuo tarpu, fotoliuminescencijos matavimai parodė ryškų juosta-juosta bei defektinių juostų emisijos slopinimą ir kvantinio našumo mažėjimą didėjant apšvitos dozei. Tai siejama su apšvitos metu susidarančiais taškiniais defektais ir defektų kompleksais, kurie sudaro papildomus energinius lygmenis medžiagos draustinėje juostoje, sustiprina nespindulinę rekombinaciją bei padidina išspinduliuotų fotonų savisugerties tikimybę.

8 Acknowledgements

I would like to express my sincere gratitude to my supervisor, Dr. Kazimieras Nomeika, for his friendly and continuous guidance, support, and genuine care throughout the entire process of this research. His advice, patience, and encouragement were essential for the successful completion of both experimental work and the preparation of this thesis.

9 Approbation

- The entire LITG and PL measurements were carried out by the author.
- All calculations and data interpretation were performed by the author.
- The entire thesis was written by the author.

10 Literature List

References

[1] T. Kawashima *et al.*, "Optical properties of hexagonal gan," *J. Appl. Phys.*, vol. 82, 1997.

[2] S. J. Pearton *et al.*, "Review—ionizing radiation damage effects on gan devices," *ECS Journal of Solid State Science and Technology*, vol. 5, 2016.

[3] E. Gaubas *et al.*, "Study of neutron irradiated structures of ammonothermal gan," *J. Phys. D: Appl. Phys*, vol. 50, 2017.

[4] R. Dwilinski *et al.*, "Bulk ammonothermal gan," *Journal of Crystal Growth*, vol. 311, pp. 3015–3018, 2009.

[5] J. G. Marques *et al.*, "Defect production in neutron irradiated gan," *Nuclear Instruments and Methods in Physics Research Section B: Beam Interactions with Materials and Atoms*, vol. 249, pp. 359–361, 2006.

[6] M. A. Reshchikov, "Measurement and analysis of photoluminescence in gan," *Journal of Applied Physics*, vol. 129, 2021.

[7] H. W. Li *et al.*, "Chip-scale gan integration," *Progress in Quantum Electronics*, vol. 70, 2016.

[8] M. Dauelsberg *et al.*, "Progress in modeling of iii-nitride movpe," *Progress in Crystal Growth and Characterization of Materials*, vol. 66, 2020.

[9] B. Monemar *et al.*, "Group iii-nitride based hetero and quantum structures," *Progress in Quantum Electronics*, vol. 24, pp. 239–290, 2000.

[10] M. Caro *et al.*, "Group-iii nitrides." `https://miguelcaro.org/wiki/index.php/Group-III_nitrides`, n.d. Accessed: 2025-05-19.

[11] B. Ambacher *et al.*, "Two dimensional electron gases induced by spontaneous and piezoelectric polarization in undoped and doped algan/gan heterostructures," *Journal of Applied Physics*, vol. 87, pp. 334–344, 2000.

[12] J. K. Sheu *et al.*, "White-light emission from near uv ingan–gan led chip precoated with blue/green/red phosphors," *Photonics Technology Letters*, vol. 15, pp. 18–20, 2003.

[13] K. Lorentz *et al.*, "Defect studies on fast and thermal neutron irradiated gan," *Nuclear Instruments and Methods in Physics Research B*, vol. 266, pp. 2780–2783, 2008.

[14] S. Suihkonen *et al.*, "Defects in single crystalline ammonothermal gallium nitride," *Advanced Electronic Materials*, vol. 3, 2017.

[15] C. Elias, "Optical spectroscopy of hexagonal boron nitride: from bulk to monolayer," *PhD Thesis*, 2022.

[16] T. Heikkinen *et al.*, "Effect of mn and mg dopants on vacancy defect formation in ammonothermal gan," *Journal of Crystal Growth*, vol. 547, 2020.

[17] J. F. Muth *et al.*, "Absorption coefficient and refractive index of gan, aln and algan alloys," *MRS Internet J. Nitride Semicond.*, 1999.

[18] T. T. Mnatsakanov *et al.*, "Carrier mobility model for gan," *Solid State Electronics*, vol. 47, pp. 111–115, 2003.

[19] R. Aleksiejūnas *et al.*, "Determination of free carrier bipolar diffusion coefficient and surface recombination velocity of undoped gan epilayers," *Appl. Phys. Lett.*, vol. 83, 2003.

[20] L. Cheng *et al.*, "Bandgap, mobility, dielectric constant, and baliga's figure of merit of 4h-sic, gan, and beta-ga2o3 from 300 to 620 k," *ACS Applied Electronic Materials*, vol. 4, 2022.

[21] W. Jiang *et al.*, "Electrical and optical properties of gallium vacancy complexes in ammonothermal gan," *Applied Physics Express*, vol. 10, 2017.

[22] J. Iveland *et al.*, "Direct measurement of auger electrons emitted from a semiconductor light-emitting diode under electrical injection: Identification of the dominant mechanism for efficiency droop," *Physical Review Letters*, vol. 110, 2013.

[23] B. Monemar, "Fundamental energy gap of gan from photoluminescence excitation spectra," *Physical Review B*, vol. 10, 1973.

[24] T. Narita *et al.*, "Effects of proton irradiation-induced point defects on shockley–read–hall recombination lifetimes in homoepitaxial gan p–n junctions," *Applied Physics Letters*, vol. 122, 2023.

[25] P. Ščajev, "Investigation of wide-bandgap semiconductor photoelectric properties by using optical techniques with temporal and spatial resolution," *Doctoral thesis*, 2013.

[26] J. K. Sheu *et al.*, "Photoluminescence spectroscopy of mg-doped gan," *Journal of Applied Physics*, vol. 84, p. 4590, 1998.

[27] E. Calleja *et al.*, "Yellow luminescence and related deep states in undoped gan," *Physical Review B*, vol. 55, 1997.

[28] M. A. Reshchikov *et al.*, "Yellow and green luminescence in a freestanding gan template," *Applied Physics Letters*, vol. 78, 2001.

[29] M. A. Reshchikov *et al.*, "Luminescence from defects in gan," *Physica B*, vol. 376-377, 2006.

[30] M. A. Reshchikov *et al.*, "Photoluminescence from gan implanted with be and f," *Physica Status Solidi (B)*, vol. 260, 2023.

[31] M. A. Reshchikov *et al.*, "Magnesium acceptor in gallium nitride. i. photoluminescence from mg-doped gan," *Phys Rev. B*, vol. 97, 2018.

[32] S. Leyre *et al.*, "Absolute determination of photoluminescence quantum efficiency using an integrating sphere setup," *Review of Scientific Instruments*, vol. 85, 2014.

[33] T. Malinauskas *et al.*, "Diffusion and recombination of degenerate carrier plasma in gan," *Phys. Status Solidi*, vol. 6, 2009.

[34] F. Tuomisto *et al.*, "Introduction and recovery of ga and n sublattice defects in electron-irradiated gan," *Phys. Rev. B*, vol. 76, 2007.

[35] T. Saxena *et al.*, "Low threshold for optical damage in algan epilayers and heterostructures," *J. Appl. Phys.*, vol. 114, 2013.

[36] D. O. Demchenko *et al.*, "Hydrogen-carbon complexes and the blue luminescence band in gan," *J. Appl. Phys.*, vol. 119, 2016.

[37] Z. Xie *et al.*, "Donor and acceptor characteristics of native point defects in gan," *J. Phys. D: Appl. Phys.*, vol. 52, 2019.

[38] J. Piprek, "Efficiency models for gan-based light-emitting diodes: Status and challenges," *Materials*, vol. 12, 2020.